

AD-A257 315



**NAVAL POSTGRADUATE SCHOOL**  
**Monterey, California**



**THESIS**

**DTIC**  
**ELECTE**  
**NOV 23 1992**  
**S E D**

**The Role of Particles in Recrystallization  
of a Thermomechanically Processed  
Al-Mg Alloy**  
by

**Stephen Andrew Rogers**

**September 1992**

**Thesis Advisor:**  
**Co-Advisor:**

**Terry R. McNelley**  
**Roy Crooks**

Approved for public release; distribution is unlimited.

**92-29926**



## REPORT DOCUMENTATION PAGE

1a. REPORT SECURITY CLASSIFICATION <b>UNCLASSIFIED</b>		1b. RESTRICTIVE MARKINGS	
2a. SECURITY CLASSIFICATION AUTHORITY		3. DISTRIBUTION/AVAILABILITY OF REPORT Approved for public release; distribution is unlimited	
2b. DECLASSIFICATION/DOWNGRADING SCHEDULE			
4. PERFORMING ORGANIZATION REPORT NUMBER(S)		5. MONITORING ORGANIZATION REPORT NUMBER(S)	
6a. NAME OF PERFORMING ORGANIZATION Mech. Engineering Dept. Naval Postgraduate School	6b. OFFICE SYMBOL (if applicable) ME	7a. NAME OF MONITORING ORGANIZATION Naval Postgraduate School	
6c. ADDRESS (City, State, and ZIP Code) Monterey, CA 93943-5000		7b. ADDRESS (City, State, and ZIP Code) Monterey, CA 93943-5000	
8a. NAME OF FUNDING/SPONSORING ORGANIZATION	8b. OFFICE SYMBOL (if applicable)	9. PROCUREMENT INSTRUMENT IDENTIFICATION NUMBER	
8c. ADDRESS (City, State, and ZIP Code)		10. SOURCE OF FUNDING NUMBERS	
		PROGRAM ELEMENT NO.	PROJECT NO.
		TASK NO.	WORK UNIT ACCESSION NO.
11. TITLE (Include Security Classification) The Role of Particles in Recrystallization of a Thermomechanically Processed Al-Mg Alloy			
12. PERSONAL AUTHOR(S) Stephen Andrew Rogers			
13a. TYPE OF REPORT Master's Thesis	13b. TIME COVERED FROM 04/92 TO: 09/92	14. DATE OF REPORT (Year, Month, Day) 1992, SEPTEMBER	15. PAGE COUNT 65
16. SUPPLEMENTARY NOTATION The views expressed in this thesis are those of the author and do not reflect the official policy or position of the Department of Defense or the United States Government.			
17. COSATI CODES		18. SUBJECT TERMS (Continue on reverse if necessary and identify by block number)	
FIELD	GROUP	SUB-GROUP	
		Aluminum-Magnesium alloys, superplasticity, particle stimulated nucleation (PSN)	
19. ABSTRACT (Continue on reverse if necessary and identify by block number)			
<p>The microstructural evolution related to the superplastic response of an Al-10Mg-0.1Zr alloy during thermomechanical processing (TMP) was studied. The TMP had been accomplished in previous work and consisted of 12 rolling passes, with reheating between each pass, to a total strain of 2.5. Quantitative data including length, aspect ratio and area of precipitated <math>\beta</math>-phase (<math>Al_8Mg_5</math>) particles were obtained using image analysis methods applied to the as-rolled conditions following passes 8, 10 and 12. The corresponding accumulated strains were 1.5, 2.0 and 2.6, respectively. Precipitation of the <math>\beta</math>-phase is complete by pass 8 and the size as well as the size distribution remained essentially unchanged in the subsequent passes. A model for particle-stimulated nucleation of recrystallization, which is based on thermodynamic considerations, is evaluated with respect to experimental data.</p>			
20. DISTRIBUTION/AVAILABILITY OF ABSTRACT <input checked="" type="checkbox"/> UNCLASSIFIED/UNLIMITED <input type="checkbox"/> SAME AS RPT. <input type="checkbox"/> DTIC USERS		21. ABSTRACT SECURITY CLASSIFICATION <b>UNCLASSIFIED</b>	
22a. NAME OF RESPONSIBLE INDIVIDUAL Terry R. McNelley		22b. TELEPHONE (Include Area Code) (408) 646-2589	22c. OFFICE SYMBOL ME/Mc

Approved for public release; distribution is unlimited

***The Role of Particles in Recrystallization  
of a Thermomechanically Processed  
Al-Mg Alloy***

by  
***Stephen Andrew Rogers***  
***Captain, United States Army***  
***B.S.M.E., Marquette University, 1983***

Submitted in partial fulfillment of the  
requirements for the degree of

**MASTER OF SCIENCE IN MECHANICAL ENGINEERING**


from the

**NAVAL POSTGRADUATE SCHOOL**  
September, 1992

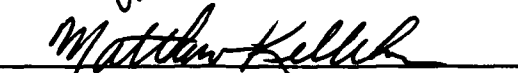
Author:

  
***Stephen Andrew Rogers***

Approved By:

  
***Terry R. McNelley, Thesis Advisor***

  
***Roy Crooks, Co-Advisor***

  
***Matthew D. Kelleher, Chairman***  
**Department of Mechanical Engineering**

## ABSTRACT

The microstructural evolution related to the superplastic response of an Al-10Mg-0.1Zr alloy during thermomechanical processing (TMP) was studied. The TMP had been accomplished in previous work and consisted of 12 rolling passes, with reheating between each pass, to a total strain of 2.5. Quantitative data including length, aspect ratio and area of precipitated  $\beta$ -phase ( $\text{Al}_3\text{Mg}_2$ ) particles were obtained using image analysis methods applied to the as-rolled conditions following passes 8, 10 and 12. The corresponding accumulated strains were 1.5, 2.0 and 2.6, respectively. Precipitation of the  $\beta$ -phase is complete by pass 8 and the size as well as the size distribution remained essentially unchanged in the subsequent passes. A model for particle-stimulated nucleation of recrystallization, which is based on thermodynamic considerations, is evaluated with respect to experimental data.

Accession For	
NTIS   CRA&I	<input checked="" type="checkbox"/>
DTIC   TAB	<input type="checkbox"/>
Unannounced	<input type="checkbox"/>
Justification .....	
By .....	
Distribution /	
Availability Codes	
Dist	Avail and / or Special
<b>A-1</b>	

**DTIC QUALITY INSPECTED 4**

## TABLE OF CONTENTS

<b>I. INTRODUCTION .....</b>	<b>1</b>
<b>II. BACKGROUND .....</b>	<b>3</b>
<b>A. ALUMINUM ALLOYS .....</b>	<b>3</b>
<b>B. STRENGTHENING MECHANISMS .....</b>	<b>3</b>
1. Solid Solution Strengthening.....	3
2. Dispersion Strengthening .....	4
3. Precipitation of the $\beta$ -phase .....	4
<b>C. DEVELOPMENT OF SUPERPLASTICITY .....</b>	<b>6</b>
1. Microstructural Prerequisites and Superplastic Deformation Mode ....	6
2. Phenomenological Equations .....	7
<b>D. MECHANISMS FOR RECRYSTALLIZATION .....</b>	<b>9</b>
1. Grain Refinement in Al-Mg Alloys .....	9
2. Particle Stimulated Nucleation of Recrystallization .....	10
<b>III. EXPERIMENTAL PROCEDURES .....</b>	<b>16</b>
<b>A. MATERIAL .....</b>	<b>16</b>
<b>B. THERMOMECHANICAL PROCESSING .....</b>	<b>16</b>
1. Solution Treatment .....	18
2. Warm Rolling .....	18
<b>C. SAMPLE PREPARATION .....</b>	<b>20</b>
1. Grinding.....	20
2. Mechanical Polishing .....	20
3. Electropolishing.....	21
<b>D. SCANNING ELECTRON MICROSCOPY .....</b>	<b>22</b>
<b>E. IMAGE ANALYSIS.....</b>	<b>22</b>
<b>IV. RESULTS AND DISCUSSION .....</b>	<b>25</b>
<b>A. MICROSCOPY.....</b>	<b>25</b>
1. As-Cast and Forged Condition .....	26

2. Pass 3 (Strain = 0.4) .....	28
3. Pass 6 (Strain = 1.0) .....	30
4. Pass 8 (Strain = 1.5) .....	32
5. Pass 10 (Strain = 2.0) .....	34
6. Pass 12 (Strain = 2.6) .....	34
B. QUANTITATIVE ANALYSIS .....	38
C. DISCUSSION .....	44
V. CONCLUSIONS AND RECOMMENDATIONS .....	47
A. CONCLUSIONS .....	47
B. RECOMMENDATIONS .....	47
APPENDIX A .....	48
LIST OF REFERENCES .....	51
INITIAL DISTRIBUTION LIST .....	53

## LIST OF TABLES

TABLE 1.	NOMINAL ALLOY COMPOSITION (wt.%).....	16
TABLE 2.	TMP 6 ROLLING SCHEDULE .....	19
TABLE 3.	NORMALIZED LENGTH TABULAR DATA .....	48
TABLE 4.	NORMALIZED ASPECT RATIO TABULAR DATA .....	49
TABLE 5.	NORMALIZED AREA TABULAR DATA .....	50

## LIST OF FIGURES

Figure 2.1	Al-Mg Phase Diagram .....	5
Figure 2.2	Schematic of Conditions for PSN .....	12
Figure 2.3	Relationship Between Critical Parameters for PSN .....	15
Figure 3.1	TMP Schematic .....	17
Figure 3.2	Schematic of Electropolishing Apparatus .....	21
Figure 4.1.a	Optical micrograph showing Al-10Mg-0.1Zr in the as-cast and forged condition following solution treatment.....	27
Figure 4.1.b	Backscattered electron micrograph showing Al-10Mg-0.1Zr in the as-cast and forged condition following solution treatment. ....	28
Figure 4.2	Backscattered electron micrograph showing Al-10Mg-0.1Zr following pass 3: a) in the as-rolled condition; b) following 30 minutes of annealing at 300 °C.....	29
Figure 4.3	Backscattered electron micrograph showing Al-10Mg-0.1Zr following pass 6: a) in the as-rolled condition; b) the same region at twice the magnification .....	31
Figure 4.3.c	Backscattered electron micrograph showing Al-10Mg-0.1Zr following pass 6 in the annealed condition.....	32
Figure 4.4	Backscattered electron micrograph showing Al-10Mg-0.1Zr following pass 8: a) in the as-rolled condition; b) following 30 minutes of annealing at 300 °C.....	33
Figure 4.5	Backscattered electron micrographs showing Al-10Mg-0.1Zr following pass 10: a) in the as-rolled condition; b) following 30 minutes of annealing at 300 °C.....	35
Figure 4.5.c	Backscattered electron micrograph showing Al-10Mg-0.1Zr following pass 10 in the annealed condition at a higher magnification. ....	36

Figure 4.6	Backscattered electron micrograph showing Al-10Mg-0.1Zr following pass 12: a) in the as-rolled condition; b) following 30 minutes of annealing at 300 °C.....	37
Figure 4.7	Normalized Length Distribution: a) Pass 8; b) Pass 10; c) Pass 12 .....	40
Figure 4.8	Normalized Aspect Ratio: a) Pass 8; b) Pass 10; c) Pass 12.....	41
Figure 4.9	Normalized Area Distribution: a) Pass 8; b) Pass 10; c) Pass 12 .....	42
Figure 4.10.a	Al-10Mg-0.1Zr $\beta$ -phase Volume Fraction versus True Strain.....	43
Figure 4.10.b	Al-10Mg-0.1Zr $\beta$ -phase Particle Length versus True Strain.....	43

## **ACKNOWLEDGEMENTS**

I would like to thank Dr. Terry R. McNelley for his generous knowledge and guidance during the course of this research. I am especially grateful to Dr. Roy Crooks for his invaluable expertise and time during the experimental phase and toward the analysis of microscopy and quantitative data. Doug Shelton and Rich Hashimoto promptly answered the call - in spite of their hectic schedules - for equipment repairs, emergency supplies and much appreciated technical advise. My fellow thesis students were extremely helpful in particular experimental procedures. Much appreciation goes to John Sedlak for his expertise in electropolishing and photography. Finally, my sincere thanks goes to my lovely wife Sheri - the most important person in this whole process - for her patience, kindness and support in helping me achieve this goal.

# **I. INTRODUCTION**

Superplasticity refers to the ability of some polycrystalline materials, given the proper conditions, to undergo large plastic deformations ( $\geq 200\%$ ) without localized necking. Although it was observed as early as 1912 by Bengough, its commercial feasibility was not appreciated until work in the former Soviet Union was recognized in 1962 [Ref. 1]. Today, superplasticity is a routinely used method for manufacturing complex parts, with Titanium and Aluminum alloys the primary materials used for commercial and defense applications.

Superplasticity does not occur naturally in metals. It requires carefully controlled alloying and thermomechanical processing (TMP) treatments to obtain a fine and stable recrystallized grain structure. Microstructural stability is usually provided by a homogeneous distribution of a second phase. The resulting microstructure may exhibit superplastic flow in specific temperature and strain rate regimes via diffusion controlled grain boundary sliding. The ability to form complex shapes eliminates or reduces the need for multi-part assemblies with associated fasteners and weldments. Thus stronger, lighter and less expensive components, often with desirable improvements in ductility, corrosion resistance and fatigue can be commercially produced.

Superplastic forming (SPF) is most commonly applied in the aircraft industry. In aircraft, the maximum advantage is gained by increasing the strength-to-weight ratio of components and reducing the number of parts and subassemblies. These factors streamline assembly operations and reduce costs.

The TMP methods used for microstructural control in this research may also have an application in the design of processes for light-weight armor materials. It is possible that a fine, equiaxed and homogeneous grain structure may enhance impact resistance and reduce spalling. Spalling is the lethal delamination and shattering of

a metal inside an armored vehicle crew compartment as a result of projectile impact. These processes and materials may have application either in secondary - add on - armor or in structural material with a primary role of armor protection.

Research into superplasticity in Al alloys has been conducted at the Naval Postgraduate School (NPS) since 1984. The initial effort [Ref. 2] was directed at developing a processing method to disperse the intermetallic  $\beta$ -phase ( $\text{Al}_3\text{Mg}_2$ ) in high-Mg, Al-Mg alloys in order to reduce their susceptibility to stress corrosion cracking (SSC). The TMP employed was successful in this respect and also resulted in a refined microstructure 0.5 to 1.0  $\mu\text{m}$  in size, suggesting the potential for superplastic behavior. Subsequent TMP and mechanical testing on a high-Mg material also containing an addition of 0.5 wt.% Mn to further refine the grain size, resulted in elongations > 400% - clearly in the superplastic range - although evidence of recrystallization was ambiguous [Ref. 3]. More recent work by Gorsuch [Ref. 4] has obtained elongations > 1000% for a processed Al-10Mg-0.1Zr alloy, in which a fully recrystallized grain structure was revealed at the conclusion of TMP. In this research, the role of the  $\beta$ -particles in the recrystallization of this alloy during TMP is studied.

## **II. BACKGROUND**

### **A. ALUMINUM ALLOYS**

Aluminum (Al) is the second most plentiful element on earth [Ref. 5]. Its most useful properties include low density, potential for heat treatment to high strength, high electrical and thermal conductivities, excellent resistance to corrosion and non-ferromagnetic qualities. In conjunction with the ability to be cast or formed by most known processes, these combinations make Al one of the most versatile materials, with exceptional potential for military, industrial and household applications. Various contaminants generally remain in commercially processed pure Al, resulting in degradation of toughness and ductility. These properties can be improved considerably through purification processes, but at significant expense. Through the addition of alloying elements and subsequent processing, however, the strength of Al can be increased beyond even that of structural steel, in a cost-effective fashion.

There are currently greater than 300 Al alloying compositions [Ref. 6], constituting a versatile range of properties dependent upon the processing method. Magnesium (Mg) is the most widely used alloying element in Al, primarily because it adds strength in solid solution while maintaining ductility. There are various ways of employing alloying elements for the purpose of strengthening Al.

### **B. STRENGTHENING MECHANISMS**

#### **1. Solid Solution Strengthening**

Solid solution strengthening is a function of atomic radii differences between solute and solvent atoms. Solute atoms fill either substitutional or interstitial sites, distorting and straining the original lattice, thus restricting dislocation movement. Mg atoms work ideally in this role due to their substantially larger size when compared to Al atoms and the high solid solubility of

Mg ( $\approx 17.4$  wt.%) [Ref. 7]. Commercially, it is a common additive (usually 0.5 - 6.0 wt.%) for strengthening purposes.

## **2. Dispersion Strengthening**

When an alloying element is added in excess of the solubility limit, the excess solute atoms form a second phase with the solvent atoms. In Al alloys, Zirconium (Zr) is relatively insoluble and forms a second phase of  $\text{ZrAl}_3$ . Where larger amounts of Zr (up to 0.5 wt.%) have been used in similar Al alloy systems, the  $\text{ZrAl}_3$  particles have been shown to inhibit grain growth after recrystallization [Ref. 8]. Due to the small amounts used in this Al-10Mg-0.1Zr material, the contribution of the Zr in solution and the  $\text{ZrAl}_3$  phase is not fully understood. This research is primarily concerned with the second phase due to the addition of Mg.

## **3. Precipitation of the $\beta$ -phase**

Precipitation strengthening occurs when second phase particles, which precipitate during an appropriate heat treatment, impede dislocation movement and increase strength. The extent of the dislocation impediment, and thereby the improvement in strength, depends on whether these particles are incoherent or continuous with the matrix lattice structure.

This phenomenon occurs only under certain conditions. The maximum solubility of the alloying agent must be on the order of several percent or greater and the phase diagram must exhibit a decreasing solubility limit with decreasing temperature, as depicted in the Al-Mg phase diagram in Figure 2.1 .

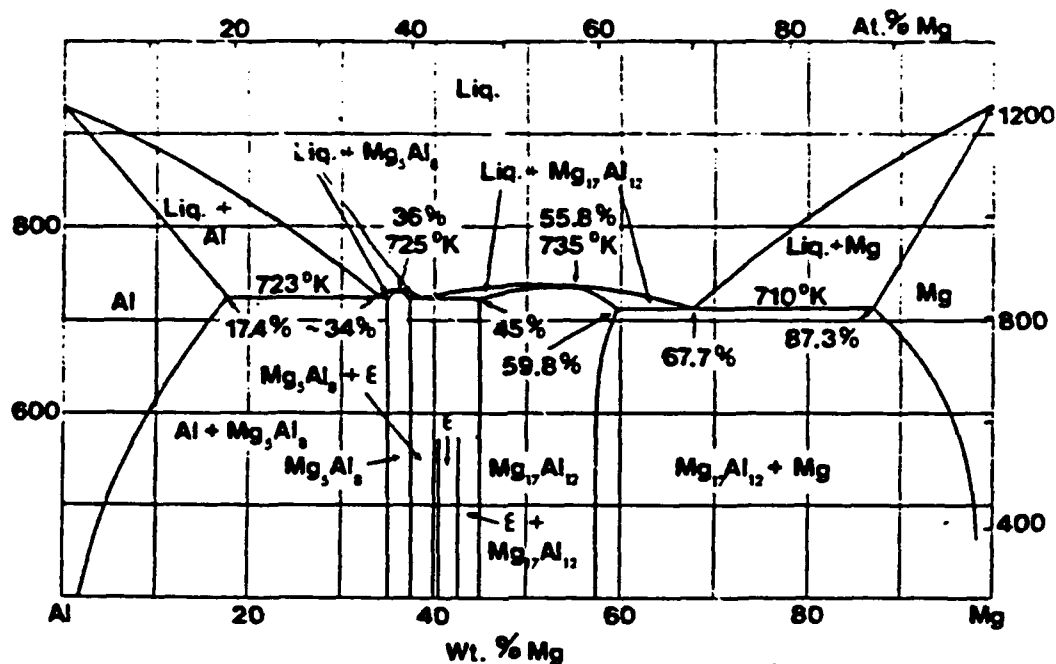
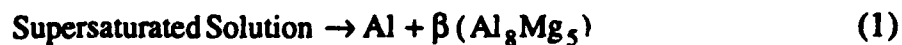


**Figure 2.1. Al-Mg Phase Diagram**

Although the Al-Mg phase diagram, in conjunction with a high solid solubility of Mg in Al, indicates the potential for precipitation strengthening, this alloy actually does not strengthen via this mechanism. The very rapid transformation of coherent  $\beta'$  to incoherent  $\beta$  during aging treatment is the first obstacle. Furthermore, these particles tend to be coarse and widely spaced. But the most severe problem is the tendency for the  $\beta$ -phase to precipitate preferentially at grain boundaries, a condition resulting in high vulnerability to intergranular cracking and stress corrosion cracking (SCC). For Al-Mg alloys, the precipitation reaction occurs according to the equation



For these reasons, the Mg concentration in Al rarely exceeds 6.0 wt.%.

Through thermomechanical processing (TMP) techniques, however, the  $\beta$ -phase can be uniformly dispersed and larger quantities of Mg (as much as 10 wt.%) can be added without encountering excessive intergranular cracking or SCC [Ref. 2]. As previously stated, these particles do not directly enhance strength, but they do play a critical role in recrystallization during TMP. Defining this role, in particular for an Al-10Mg-0.1Zr alloy which exhibits a refined grain size and is highly superplastic after TMP, is the intent of this research.

### **C. DEVELOPMENT OF SUPERPLASTICITY**

Earlier, superplasticity was briefly introduced, emphasizing the refined grain structure and the processing methods to achieve it. Several other important features of a superplastic microstructure are relevant and will be discussed here.

#### **1. Microstructural Prerequisites and Superplastic Deformation Mode**

Grain boundary sliding is the primary mode of plastic deformation during straining of superplastic materials. Several microstructural features are necessary for the activation of this mode. Foremost is a refined, equiaxed grain structure. Typically, fine grains  $\leq 10 \mu\text{m}$  in size are necessary in order to achieve superplastic elongations. To attain large superplastic responses this equiaxed, refined grain structure must be maintained throughout the straining process. Thus, grain boundary migration is essential, providing a further means of relieving stresses, and preventing the elongation of grains with the subsequent degradation of superplasticity. [Ref. 1]

Furthermore, high angle grain boundaries ( $\geq 15^\circ$  in misorientation) are essential for grain boundary sliding. As the misorientation angle between grains increases, the boundary becomes more disordered and atomic registry decreases. This allows the adjacent grains to slip due to the presence of shear stresses. The greater the boundary misorientations, the better the superplastic response. [Ref. 1]

The presence of a second phase is the key to maintaining the microstructure discussed above. With the appropriate distribution and spacing, second-phase particles may retard grain growth and stabilize the microstructure during superplastic flow. In Al-Mg alloys, the  $\beta$ -phase is  $\text{Al}_8\text{Mg}_5$ . The  $\beta$ -phase particles are hard at ambient temperature, but soften at the superplastic forming (SPF) temperature  $\approx 300^\circ\text{C}$  [Refs. 8 and 9]. The deformation of  $\text{Al}_8\text{Mg}_5$  during SPF may be important to the prevention of cavitation.

## 2. Phenomenological Equations

To obtain superplastic flow in a material, the tendency for localized necking during tensile deformation must be inhibited. The susceptibility of a material to localized necking is related to its strain rate sensitivity,  $m$ :

$$m = \frac{\partial \ln \sigma}{\partial \ln \dot{\epsilon}} \quad (2)$$

where  $\sigma$  is the flow stress and  $\dot{\epsilon}$  is the strain rate. When stress versus strain rate data for a superplastic material are plotted as  $\ln \sigma$  versus  $\ln \dot{\epsilon}$ , the resulting curve will be sigmoidal and the slope will provide values of  $m$  according to Equation (2). If the elongation to failure is likewise plotted against  $\ln \dot{\epsilon}$ , the maximum elongation is often associated with a slope,  $m$ , of 0.5. Fine-grained superplastic alloys usually exhibit this value of  $m$ , and as  $m$  increases, the superplastic response improves due to strain-rate hardening in the necked region. When  $m$  is equal to 1, a material is ideally superplastic, and behaves in a Newtonian-viscous manner, whereby diffusional flow dominates and no localized necking occurs. [Ref. 1]

The strain rate,  $\dot{\epsilon}$ , has been shown to be a function of a material's grain size and diffusional properties according to:

$$\dot{\epsilon} \propto \frac{D_{eff}}{\delta^2} (\sigma/E)^2 \quad (3)$$

Here,  $D_{eff}$  is the effective diffusion coefficient,  $\delta$  is the grain size,  $\sigma$  is the flow stress, and  $E$  is the modulus of elasticity. The exponent value of 2 is the strain-rate hardening coefficient,  $n$ , derived from  $n = 1/m$ , where  $m = 0.5$  as discussed previously. Equations (2) and (3) reveal that a decreasing grain size is associated with an increasing superplastic strain rate. This is the analytical evidence to support the requirement of a fine grain size for superplasticity.

Diffusional processes control the superplastic response. It is believed that superplastic flow is governed by a combination of grain boundary diffusion,  $D_{gb}$ , and lattice self-diffusion,  $D_L$ , according to:

$$D_{eff} = D_L f_L + D_{gb} f_{gb} \quad (4)$$

where  $f_L$  and  $f_{gb}$  are the fractions of atoms associated with lattice and grain boundary diffusion, respectively. If  $f_L = 1$  and  $f_{gb} = \pi w/\delta$ , this equation becomes

$$D_{eff} = D_L + D_{gb} \left( \frac{\pi w}{\delta} \right) \quad (5)$$

where  $w$  is the grain boundary width. This indicates that a transformation occurs from lattice diffusion to grain boundary diffusion as the grain size decreases. The grain boundaries must be of high misorientation angle in order to support such diffusional processes. The complete details and the actual contribution from each diffusion process are not yet fully understood. [Ref. 1]

## **D. MECHANISMS FOR RECRYSTALLIZATION**

A fine recrystallized grain structure is essential to attaining a high strain rate which drives the superplastic response in a material. Initial research at NPS was oriented toward processing methods to produce this refined grain structure. More recent work has attempted to define the mechanism for this recrystallization during TMP.

### **1. Grain Refinement in Al-Mg Alloys**

The first attempt [Ref. 11] to understand the recrystallization mechanism in Al-Mg alloys invoked the finely dispersed  $\beta$ -phase as a stabilizing structure during continuous recrystallization (CRX). In this model, recovered substructures with characteristic low-angle grain boundaries form during the initial annealing cycles of the TMP. The presence of a finely dispersed  $\beta$ -phase retards dislocation motion and stabilizes these substructures as the boundary misorientation progressively increases during subsequent rolling/annealing cycles and a refined structure develops. Although superplastic responses were attained, determining the extent of the recrystallization from TEM and misorientation data was difficult.

Further work [Ref. 12] applied newer techniques to the analysis of the resulting grain structure. Backscattered electron imaging - to enhance orientation contrast and obtain data from bulk samples of material - identified deformation zones as bright contrast regions adjoining individual particles in as-rolled Al-10Mg-0.1Zr material. Annealing for 30 minutes at 300 °C revealed grains associated with intergranular particles and a grain size approximately equal to the interparticle spacing. This new data strongly suggested particle-stimulated nucleation (PSN) of recrystallization was occurring and was responsible for a fine grain structure and higher elongation. Particle coarsening would be expected with increased interpass annealing, and as this occurs during the TMP, enough could eventually reach a

critical diameter,  $d_{cr}$ , at which PSN of recrystallization would occur. The particle size was not evaluated quantitatively, but did not appear to conform to this expectation. An average particle size of 1  $\mu\text{m}$  or greater is generally considered necessary for PSN [Ref. 13].

## 2. Particle Stimulated Nucleation of Recrystallization

Particles stimulate and/or retard recrystallization depending on their size distribution, spacing and coherency [Ref. 14]. It is these factors, combined with the reduction per pass and strain accumulated, which determine whether PSN can occur and, ultimately, the rate of recrystallization during processing.

The interaction between a particle, its deformation zone and the surrounding matrix is extremely complex. This process has been studied by many and numerous approaches have been taken. Humphreys, et al. [Refs. 13, 15, 16 and 17] has clearly shown recrystallization associated with the deformation zones surrounding particles and with highly misoriented substructures within these zones which appear to serve as nucleation sites.

The details of how the deformation zones form around the particles are not fully understood. However, a thermodynamic approach to this problem has been summarized by Williams and Stark [Ref. 14] following work done by Argon, et al. [Ref. 18]. This study showed that the size of the deformation zone,  $\lambda$ , is related to the particle diameter,  $d_p$ , and the true strain,  $\epsilon$ , by

$$\lambda = A d_p \epsilon^{\frac{n}{n+1}} \quad (6)$$

where

$$A = \frac{K\sqrt{2}}{8\tau_{cr}} \cdot \left[ \frac{4\tau_{cr}^{(n+1)}}{\sqrt{2nK}} \right]^{\left(\frac{n}{n+1}\right)} \quad (7)$$

Here,  $\tau_{cr}$  is the critical resolved shear stress required to move dislocation loops away from the particle. The strain hardening coefficient,  $n$ , and the material constant,  $K$ , are the same used in Ludwik's and Hollomon's strain-hardening relationship,  $\sigma = K\epsilon^n$ . The constant,  $A$ , describes the strain hardening behavior of the matrix.

Equation (6) indicates that a larger particle produces a larger deformation zone. This model does not depict the detailed microstructural features of the deformation zone [Refs. 13 and 17]. Instead, particles are considered spherical and nondeformable, and the deformation zone uniformly surrounds the particle as shown in Figure 2.2. In processing at ambient temperature, which this model assumes, this is a reasonable assumption. But at elevated processing temperatures, particles may be deformable [Refs. 8 and 9] and not equiaxed, and thus the interaction will be even more complex.

If stored strain energy provides the driving process for PSN, then the critical nucleus size,  $\delta_{cr}$ , must at least be as small as the size of the deformation zone,  $\lambda$ , surrounding a particle. According to Nes [Ref. 19], the value of  $\delta_{cr}$  necessary for recrystallization in this model is:

$$\delta_{cr} = \frac{4\gamma}{E} \quad (8)$$

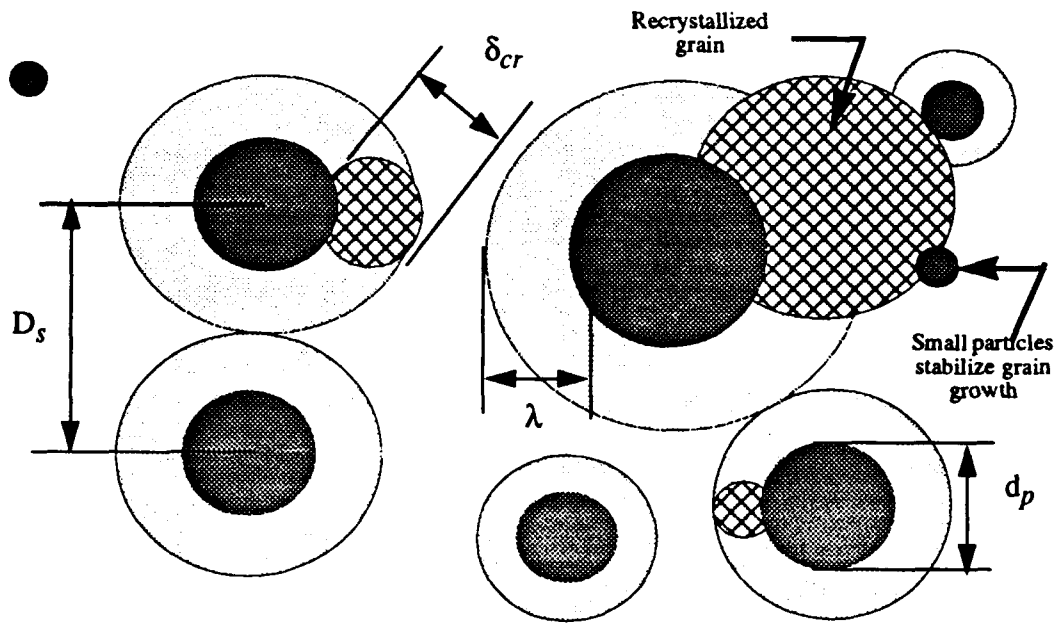


**Figure 2.2. Schematic of Conditions for PSN**

where  $\gamma$  is the grain boundary interfacial energy and  $E$  is stored strain energy in the matrix ( $E \approx \rho G b^2$  where  $\rho$  is the dislocation density,  $G$  is the shear modulus, and  $b$  is the Burger's vector). The calculation of this equation is based on the change in volume and surface free energy associated with an embryotic grain.

Assuming that  $\lambda = \delta_{cr}$  is the appropriate condition for recrystallization and substituting  $\lambda$  from Equation (6) into  $\delta_{cr}$  from Equation (8), the critical particle diameter,  $d_{cr}$ , for recrystallization becomes:

$$d_{cr} = \frac{4\gamma}{E} \cdot \left[ 2A\epsilon^{\left(\frac{n}{n+1}\right)} + 1 \right]^{-1} \quad (9)$$

An analysis of this model reveals that as  $\epsilon$  accumulates during processing,  $d_{cr}$  decreases as a result of a larger  $\lambda$  and more stored energy in the form of increased dislocation density. The value of  $d_{cr}$  also decreases as  $\gamma$  decreases. Thus, substructures of low boundary energy  $\gamma$  could still form in association with smaller particles.

Equation (9) was developed with the assumption of straining at low temperatures, whereas the Al-10Mg-0.1Zr alloy in this research underwent TMP at higher temperatures. Thus, recovery processes which would have the effect of removing some dislocations prior to the onset of recrystallization and reducing the accumulated strain, are not incorporated into this model. Furthermore, this model of nucleation within the deformation zone only considers thermodynamics, and essentially assumes that if a zone exists then a grain will nucleate. The kinetics related to the growth of a zone are not discussed. Nevertheless, the model presents a fairly straight forward approach which, if carefully invoked, may be able to provide values for  $d_{cr}$ .

As a particle coarsens during TMP and reaches the critical size defined in Equation (9), then the nucleus within the deformation zone becomes capable of expanding into the matrix, and conditions for PSN of recrystallization exist at that particle. Assuming the particle distribution is modelled as a cubic lattice, that enough strain accumulates and that enough particles of the same size satisfy  $d_{cr}$ , then the grain size,  $\delta$ , becomes equal to the interparticle spacing,  $D_s$ :

$$\delta \approx D_s \approx \frac{d_p}{V_f^{1/3}} \quad (10)$$

where  $V_f$  is the  $\beta$ -phase volume fraction. If  $V_f \approx 0.1$ , which is the approximate  $\beta$ -phase volume fraction in Al-10Mg-0.1Zr processed at 300 °C, then Equation (10) becomes:

$$\delta \approx 2d_p \quad (11)$$

If the grain size is approximately equal to the interparticle spacing then PSN is the likely mechanism of recrystallization.

Alternatively, if Zener pinning [Ref. 15] of grain boundaries limits the grain size, then

$$\delta_{\text{Zener}} = \frac{2d_p}{3V_f} \quad (12)$$

and for  $V_f \approx 0.1$  the grain size would be:

$$\delta_{\text{Zener}} \approx 7d_p \quad (13)$$

The grain size predicted by the Zener model is three times that of the PSN limit and will exceed the interparticle spacing. It is unlikely that PSN has occurred under such circumstances.

A simplified graph of the relationship between  $d_{cr}$  and the strain,  $\epsilon$ , is represented in Figure 2.3. This graph reveals that  $d_{cr}$  decreases with increasing  $\epsilon$ , as suggested by Equation (9). The appropriate value of  $\epsilon$  is not clearly defined because, as previously stated, the effect of recovery during processing on accumulation of strain energy is unknown.

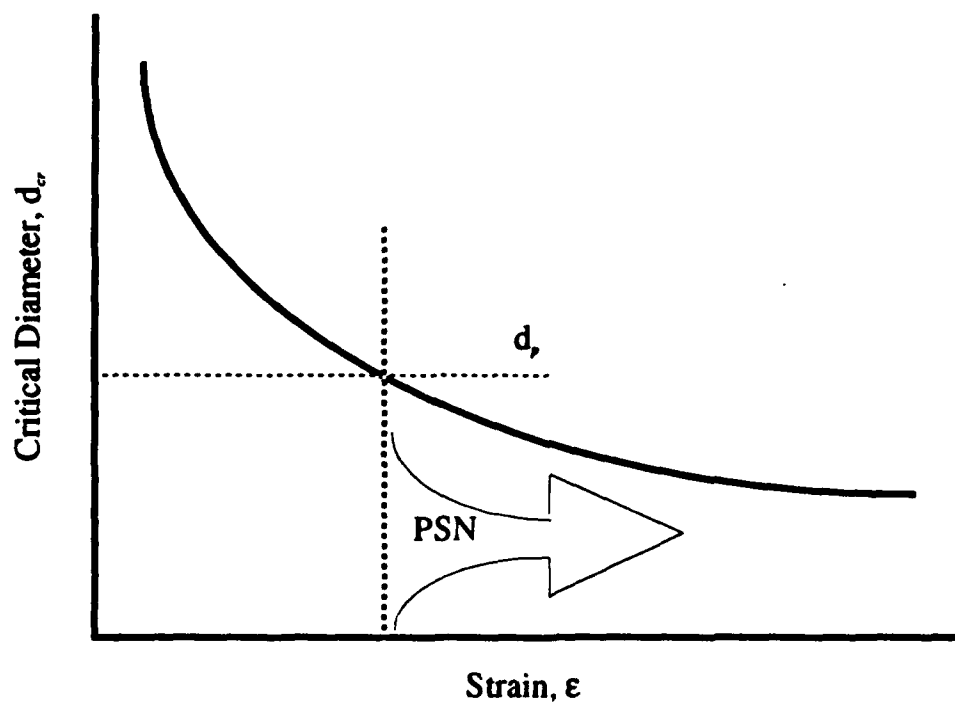


**Figure 2.3. Relationship Between Critical Parameters for PSN**

### III. EXPERIMENTAL PROCEDURES

Initial processing on Al-Mg alloys with various Mg contents was performed by Coleman [Ref. 20] in previous research at the Naval Postgraduate School. The TMP of the Al-10Mg-0.1Zr material described in this chapter was completed by Coleman and samples which were analyzed in this research were from that material.

#### A. MATERIAL

The starting material was provided by the ALCOA Technical Center, ALCOA Center, Pennsylvania as a direct-chill cast ingot (# S572826) with nominal composition of Al-10Mg-0.1Zr wt.%. The actual chemical composition is shown in Table 1.

TABLE 1: NOMINAL ALLOY COMPOSITION (wt.%)

CASTING #	Mg	Zr	Si	Fe	Ti	Be	Al
S572826	9.89	0.09	0.02	0.02	0.01	0.003	Balance

The cylindrical ingot, 150mm diameter by 580mm length, was sectioned longitudinally into 95.3mm x 31.8mm x 31.8mm rectangular billets for further processing. [Ref. 20]

#### B. THERMOMECHANICAL PROCESSING

TMP of this material was conducted according to the schematic in Figure 3.1. This procedure was developed to provide refined microstructures through control of  $\beta$ -phase precipitation during the rolling portion of the TMP.

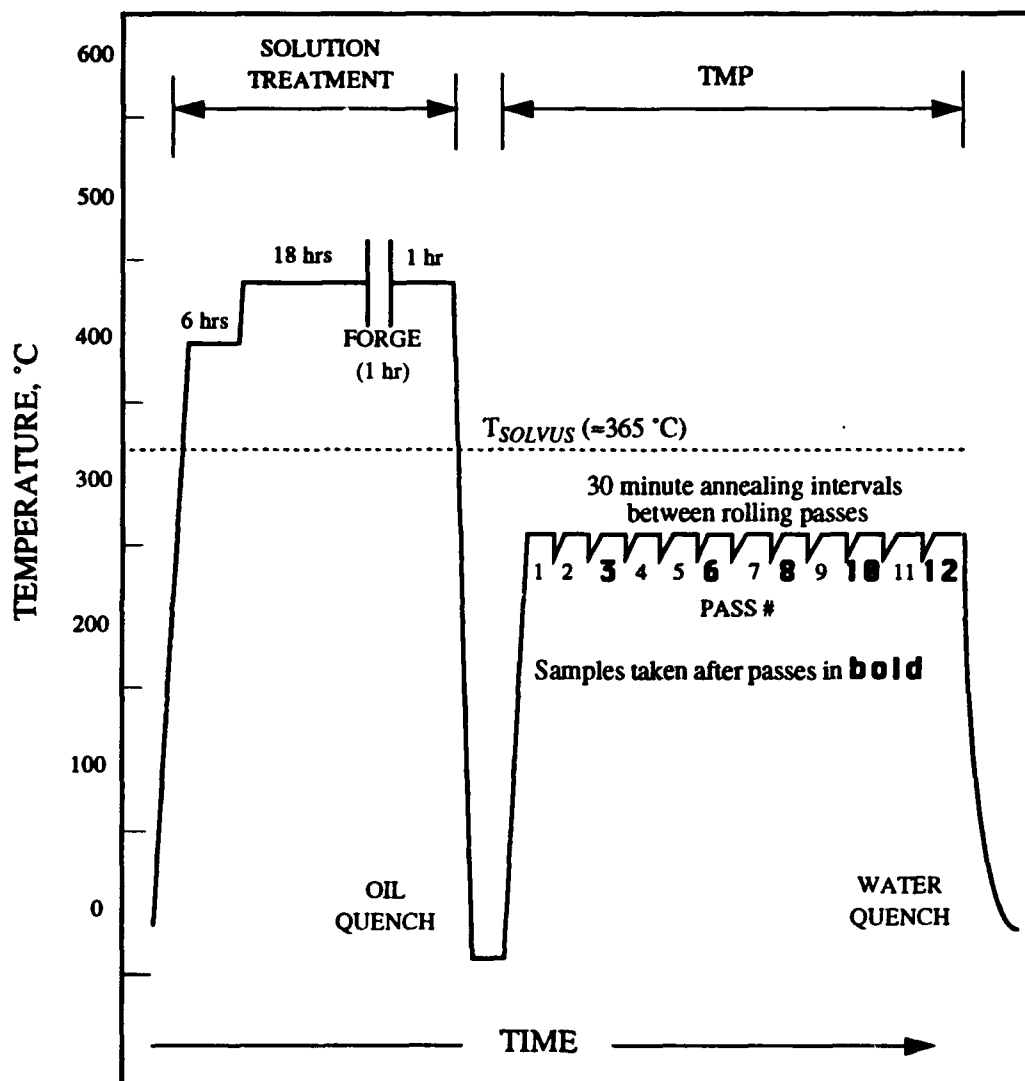


Figure 3.1. TMP Schematic

## **1. Solution Treatment**

The rectangular billet was homogenized for six hours at 440 °C, followed by solution treatment for 18 hours at 480 °C in a Lindberg type B-6 heavy duty furnace. The billet was upset forged at 440 °C along the longitudinal axis in a Baldwin-Tate-Emery testing machine equipped with platens preheated to 440 °C. The reduction ratio was 3.75:1, resulting in a billet approximately 25.4 mm thick and roughly 70 mm x 70 mm square. The true strain in forging was  $\approx 1.1$ . The billet was further solution treated at 480 °C for one hour to ensure a uniform temperature above the solvus. After oil quenching for one minute, the billet was cut in half transversely to facilitate the warm rolling stage. [Ref. 20]

## **2. Warm Rolling**

Finally, the billet was warm-rolled at 300 °C through twelve successive rolling/annealing cycles to an additional strain of 2.6. The rolling schedule used is shown in Table 2. This schedule, a modified version of that used by Gorsuch [Ref. 4] gradually increases the strain from  $\approx 10\%$  for pass 1 to  $\approx 25\%$  for pass 6 and all subsequent passes, with intermediate anneals of 30 minutes.

Before rolling commenced, the billet was heated at 300 °C for 30 minutes in an electric Blue M Furnace, model 8655F-3. Near isothermal conditions were maintained by monitoring the temperature of a steel plate under the billet with a digital thermometer (Newport Laboratory model # 267B-KCL).

Billets were rolled using a Fenn Laboratory rolling mill with roll diameters of 4.0 inches rotating at 0.327 rad/sec. After passes 3, 6, 8, 10, and 12 a sample of the rolled billet was cut (for later microstructural analysis) using a Rockwell model 724 Portable Band Saw, and then quenched in water at room temperature. Each of these samples was further sectioned in half, with one section receiving a 25 minute anneal at 300 °C. Approximately one minute was taken to

remove the billet from the oven, roll it, measure its thickness with a micrometer, cut a sample off the end, and return the rolled billet to the oven. Although the rollers were not heated and the billet was essentially air cooled between the anneals, the effect on microstructural properties is expected to be minor. [Ref. 20]

**TABLE 2: TMP 6 ROLLING SCHEDULE**

PASS	MILL GAP (in)	$t_i$ (in)	$t_f$ (in)	$\Delta t$ (in)	MILL DEFLECTION (in)	$e_i$	$\epsilon_i$	$\Sigma \epsilon_i$
1	0.900	1.065	0.941	0.124	0.041	0.116	0.124	0.124
2	0.790	0.941	0.823	0.118	0.033	0.125	0.134	0.258
3	0.680	0.823	0.712	0.111	0.032	0.135	0.145	0.403
4	0.570	0.712	0.604	0.108	0.034	0.152	0.165	0.567
5	0.460	0.604	0.500	0.104	0.040	0.172	0.189	0.756
6	0.350	0.500	0.383	0.117	0.033	0.234	0.267	1.023
7	0.265	0.383	0.299	0.084	0.034	0.219	0.248	1.270
8	0.195	0.299	0.234	0.065	0.039	0.217	0.245	1.515
9	0.140	0.234	0.174	0.060	0.034	0.256	0.296	1.812
10	0.100	0.174	0.138	0.036	0.038	0.207	0.232	2.043
11	0.070	0.138	0.104	0.034	0.034	0.246	0.283	2.326
12	0.047	0.104	0.079	0.025	0.032	0.240	0.275	2.601

## **C. SAMPLE PREPARATION**

### **1. Grinding**

The transverse-longitudinal (T-L) surfaces of the as-rolled and annealed samples extracted following passes 3, 6, 8, 10, and 12 were prepared for scanning electron microscopy. The samples were cut to size (one square centimeter or less) with a SBT-Model 650 Low Speed Diamond Saw. The T-L surface was ground using successive 240, 320, 400, and 600 grit wet-dry sand paper first applying medium- and then light - pressure strokes at each stage. Approximately twice as much time was spent on each succeeding grit, with an additional 40 to 50 very light pressure strokes applied on the 600 grit paper to complete the grinding.

### **2. Mechanical Polishing**

Each sample was successively polished with 6  $\mu\text{m}$  (Cat. No. 40-6272) and 1  $\mu\text{m}$  (Cat. No. 40-6264) Buehler Metadi Aerosol Diamond Compound using a variable-speed twelve-inch polishing wheel. The 6  $\mu\text{m}$  polish was performed on a Buehler TEXMET Polishing Cloth (Cat. No. 40-7622) using a wheel speed of 400 rpm. The 1  $\mu\text{m}$  polish was performed on a Buehler CHEMOMET Polishing Cloth (Cat. No. 40-7922) at 200 rpm. A gradually decreasing medium to very light pressure was applied while slowly moving each sample clockwise against the rotational direction of the wheel. Between five and ten minutes of polishing per wheel was generally deemed adequate, depending on the sample. Each sample was intermittently inspected by rinsing in methanol, washing very carefully with a mild Alconox Detergent, rinsing again in methanol and thoroughly drying under a Buehler TORRAMET Specimen Dryer.

At a minimum, all 6  $\mu\text{m}$  scratches should be removed during the 1  $\mu\text{m}$  polish. Very minor 1  $\mu\text{m}$  scratches can be removed during electropolishing.

### 3. Electropolishing

The electropolishing apparatus was set up as shown in Figure 3.2. A solution of 90% 2-Butoxyethanol and 10% Hydrochloric Acid, maintained at 0-1 °C, was used for electropolishing. A voltage of 14-16 VDC was applied for 2-1/2 to 3-1/2 minutes, resulting in an average current of 0.02 amps. The size of the sample surface, the number of rolling passes, and whether the as-rolled or annealed condition was being prepared all affected the polishing response to varying degrees. To attempt to quantify these would be misleading since no consistent pattern developed. The best method of determining the electropolish condition was to intermittently remove, observe and quickly return the sample to the electropolish solution. It is important to store the electropolishing solution and methanol in clean glass containers rather than in polyethylene bottles. This prevents surface contamination from obscuring the backscatter electron image in the SEM.

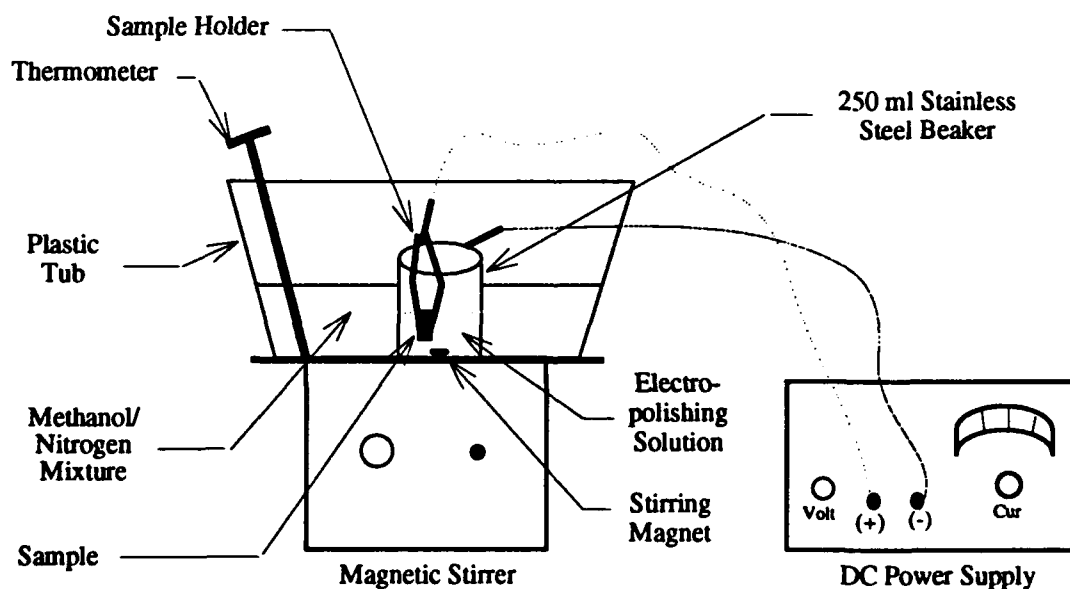


**Figure 3.2. Schematic of Electropolishing Apparatus**

## **D. SCANNING ELECTRON MICROSCOPY**

A Cambridge Model S200 scanning electron microscope equipped with a Tungsten filament was used at an accelerating potential of 20 keV. Secondary electron imaging techniques were employed to collect data for subsequent imaging analysis. Backscatter techniques, which enhance both phase and orientation contrast in this alloy, were used to examine the microstructure of the as-rolled and annealed samples.

## **E. IMAGE ANALYSIS**

Image analysis was performed to characterize the  $\beta$ -phase particles in the as-rolled conditions for passes 8, 10 and 12. The Image-Pro II Image Processing System, Version 2.0, and the Microscience ImageMeasure System were utilized in this process. The system operates by digitizing the video image of a micrograph into picture elements, or pixels. Each pixel has an associated intensity in the range from zero (dark or black) to 255 (bright or white). The range between is considered "gray level". The range of values representing an image will depend on the contrast. The objective is to maximize the contrast - dark, sharply defined particles on a bright, uniform background - to obtain the most accurate data.

Parameters such as X-difference, Intensity difference and Threshold difference are established by the operator. X-difference is the distance (in pixels) over which the intensity gradient is calculated. The Intensity difference is the minimum difference in intensity over the X-difference necessary to identify the presence of an object. Once the object is detected, the Threshold difference establishes the actual intensity value which defines the edge of an object. Both the Intensity and Threshold difference were set to Ratio mode, in which the value is calculated as a percentage of the background intensity level. Thus, the accuracy for detecting objects in a nonuniform background is improved.

The image is scanned according to these settings, and the outline of detected particles is displayed on the screen. Adjustments and editing can be performed in order to produce a very accurate overlay of the  $\beta$ -phase particles. Secondary electron images were used because of uniform background contrast. Magnifications of between 6.0 kX and 8.0 kX enabled most particles to be detected, while still maintaining sufficient working distance to obtain a statistically accurate sampling of the data. Five to nine micrographs were used per pass to further enhance the accuracy.

The normalized distribution of length, area, perimeter and aspect ratio for passes 8, 10 and 12 was generated. Length is the maximum length of a chord rotated incrementally (every  $1\frac{1}{2}^\circ$ ) through  $180^\circ$  within a particle. The area is based on the number of pixels interior to and under an object boundary. If any interior pixels are less than the threshold level, they will not be included in the area calculation; thus, holes in an object are accounted for. Perimeter is defined as the sum of line segments - using the Pythagorean Theorem to calculate the length of each segment - between vertices which are applied to an object during scanning. Aspect Ratio is the maximum length, determined as above, divided by the y-axis width.

Data were generated tabularly and in the form of histograms. Each bar on a histogram represents the number of values that are less than or equal to the "upper class limit" and greater than the "lower class limit". The upper limit of each class is labelled underneath the bar, while the lower limit is the upper limit of the previous class.

The range of the data in a histogram is established by the operator. The number of class intervals, however, is automatically set at 32. This value is based on the CGA card employed in the original software program, which limits the number of characters that can be displayed on the computer monitor screen. When dealing with

a large number of data, the number of class intervals is usually defined by the Sturgis rule [Ref. 21]:

$$N = 1 + 3.3 \log n \quad (14)$$

where  $N$  is the number of intervals and  $n$  is the number of data points. According to Equation (14), the number of class intervals should be approximately 10 - 11 for the data obtained in this research. By downloading the data into an ASCII file, and entering this file into a spreadsheet program, the class interval can be manipulated to conform with the Sturgis rule. Because of time constraints, this was not done in this research. The histograms presented are based on the default value of 32 even intervals, and although they are slightly noisy, the general distribution is sufficiently smooth to accurately reveal trends.

## IV. RESULTS AND DISCUSSION

Most of the work in superplasticity at NPS has involved mechanical testing and microstructural analysis of the fully processed material. Through juggling of process parameters - altering the number of passes and the interpass annealing time - the TMP schedule was modified numerous times in attempts to improve the superplastic response. The first systematic study of the effects of processing parameters on microstructural evolution and superplasticity was commenced by Gorsuch [Ref. 4], and the microstructure and superplastic response of Al-10Mg-0.1Zr at strains of 1.9 and 2.5 as influenced by the reheating interval were analyzed. Lyle [Ref. 22] conducted a more extensive analysis of an Al-10Mg-0.1Zr alloy, comparing microstructural and hardness data from various passes of three different TMP schedules. Subsequently, the effort has sought to define the microstructural evolution related to superplasticity from the TMP 6 schedule as a function of processing strain. Coleman [Ref. 20] was the first to study this. A microstructural analysis by backscattered electron imaging techniques, and hardness testing, of 8 wt.% Mg and 10 wt.% Mg Al binary alloys, processed according to TMP 6, was initiated.

This work represents a continuation of Coleman's efforts and introduces the quantitative image analysis of microstructural data. These data, obtained from the as-rolled conditions of passes 8, 10 and 12, provide important insight into the role of  $\beta$ -particles in recrystallization of Al-Mg alloys.

### A. MICROSCOPY

All of the samples analyzed were prepared by Coleman [Ref. 20] in previous work at NPS. Although Coleman had obtained some microscopy results for passes 3

and 12, all of the microscopy presented in this research represents the effort of the author.

The microstructure of the Al-10Mg-0.1Zr was analyzed using the backscattered electron imaging mode on the scanning electron microscope. Micrographs were taken of the as-homogenized material, as well as the as-rolled and annealed condition following passes 3, 6, 8, 10 and 12. An as-rolled sample represents the microstructure of the material immediately after the rolling process, while an annealed sample represents the microstructure just before the subsequent rolling pass.

### **1. As-Cast and Forged Condition**

Figure 4.1.a is an optical micrograph of the as-cast and forged condition after completion of homogenization. The microstructure reveals remnants of dendritic segregation of Mg from the as-cast condition. This suggests that the solution treatment may have been incomplete. Backscattered electron imaging of the same surface, as shown in Figure 4.1.b, provides no further evidence of this segregation, indicating that only minor, if any, segregation remains and that the features in Figure 4.1.a may be remnants of prior segregation or etching artifacts.

Figure 4.1.b also reveals a large, recrystallized grain as evidenced by what appears to be a migrating grain boundary. Recovered substructures in the adjacent grain indicate an incompletely recrystallized microstructure which may be relevant to the inhomogeneous aspects of  $\beta$ -phase precipitation in the early stages of the subsequent TMP.

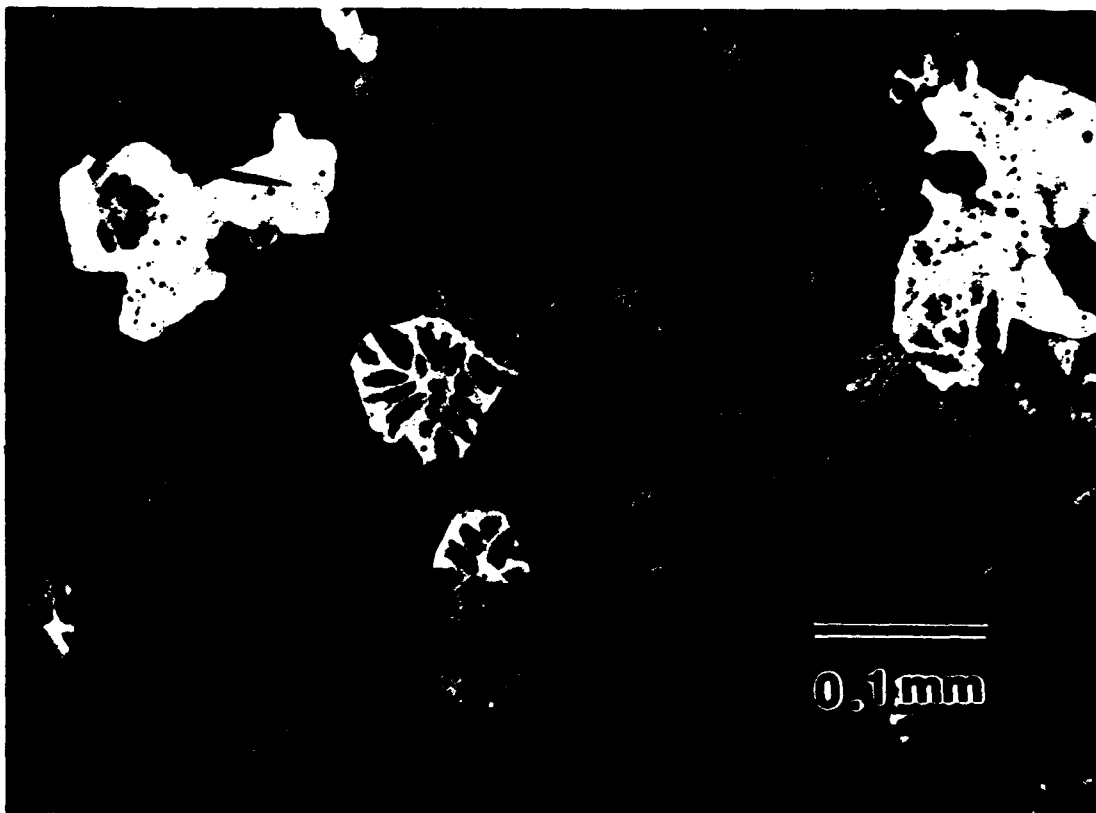


**Figure 4.1.a. Optical micrograph showing Al-10Mg-0.1Zr in the as-cast and forged condition following solution treatment**



**Figure 4.1.b. Backscattered electron micrograph showing Al-10Mg-0.1Zr in the as-cast and forged condition following solution treatment.**

## **2. Pass 3 (Strain = 0.4)**

The inhomogeneous aspects of  $\beta$ -phase precipitation are shown in the as-rolled condition in Figure 4.2.a. Continuous precipitation occurs first along grain boundaries. Additional precipitation occurs in the form of more discrete, discontinuous particles along microbands which had formed at approximately  $\pm 35$  degrees to the rolling direction during the rolling pass. The nature of these microbands, shown in Figure 4.2.b, has not been determined. Probably, they are twins; but further analysis of misorientation data must be conducted to fully understand their origin.



**Figure 4.2.** Backscattered electron micrograph showing Al-10Mg-0.1Zr following pass 3: a) in the as-rolled condition; b) following 30 minutes of annealing at 300 °C.

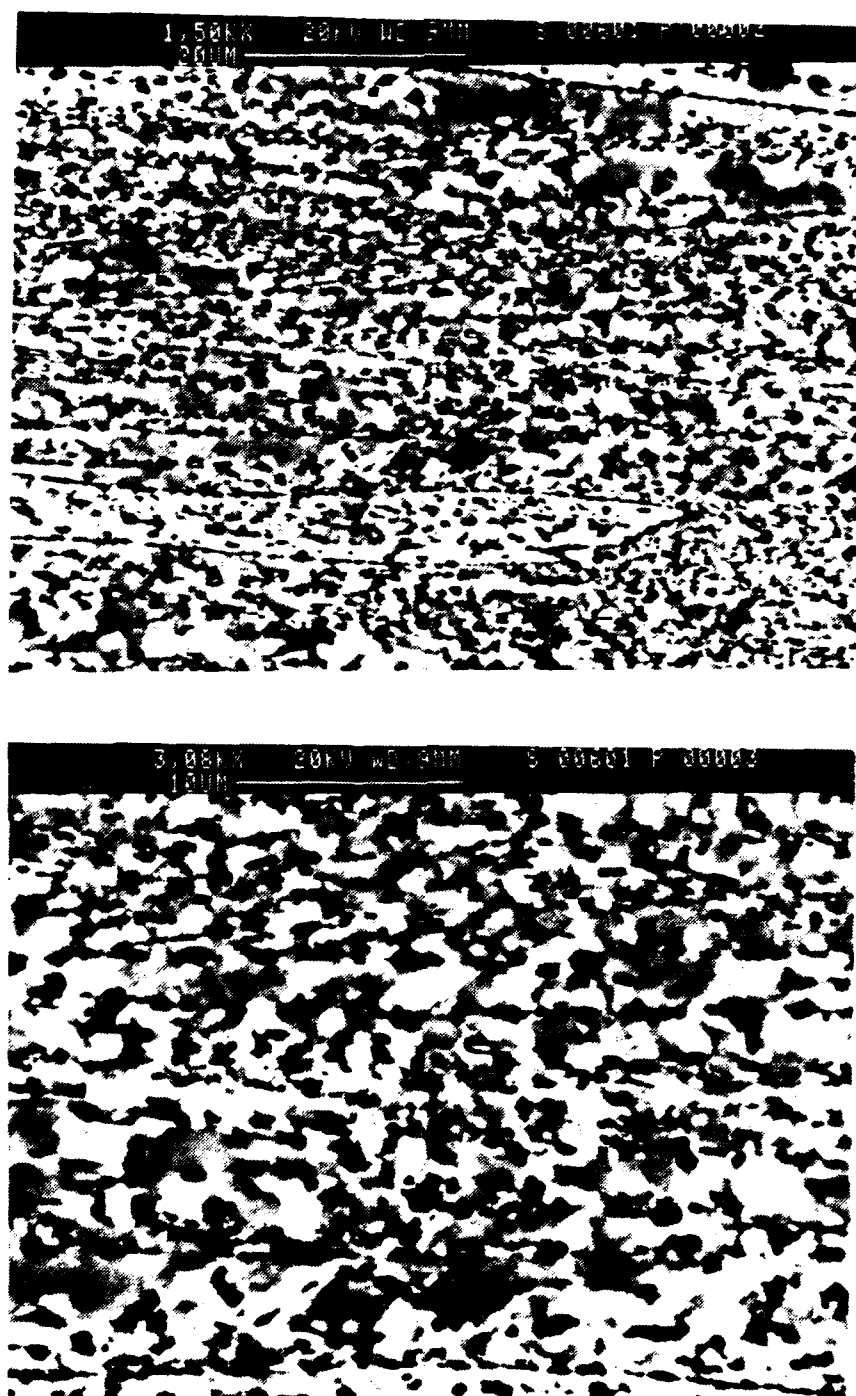
These microbands are distinguished from the long, linear, narrow slip bands shown in Figure 4.2.a. These slip bands are oriented  $\pm 45$  degrees to the rolling direction, and are much less frequently associated with precipitation. The same micrograph reveals what appears to be a subgrain structure similar to that seen in Figure 4.1.b. Microbands are rarely observed in grains where this subgrain structure exists. This accounts significantly for the nonuniform precipitation during the early passes of the TMP, which in turn explains the long TMP schedule required to attain a homogeneous distribution of  $\beta$ -phase.

### **3. Pass 6 (Strain = 1.0)**

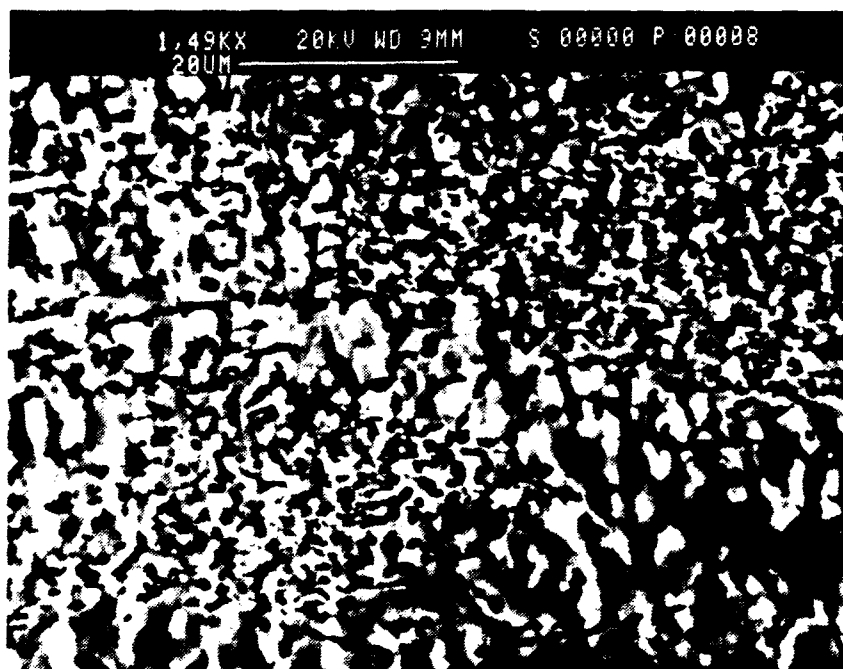
As the TMP progresses, prior first order microbands begin to flatten out and orientate toward the rolling direction, as shown in the as-rolled condition in Figure 4.3.a. Much more of the  $\beta$ -phase has precipitated and its distribution is becoming progressively more homogeneous. Through a process of spheroidization, continuous and elongated particles are becoming more discrete and sphere-like.

Figure 4.3.b reveals the same microstructure at twice the magnification of Figure 4.3.a. Between previous microband boundaries, new, higher order microbands - they may also be slip bands - have formed, but are much shorter in length than previously. Between more closely spaced particles the microbands apparently can no longer form, and more equiaxed substructures are now apparent.

In the annealed condition shown in Figure 4.3.c, microbands begin to exhibit the formation of more equiaxed, recovered substructures within their length. Where the  $\beta$ -particle density is high, only very fine, equiaxed substructures have formed.



**Figure 4.3.** Backscattered electron micrograph showing Al-10Mg-0.1Zr following pass 6: a) in the as-rolled condition; b) the same region at twice the magnification



**Figure 4.3.c. Backscattered electron micrograph showing Al-10Mg-0.1Zr following pass 6 in the annealed condition.**

#### **4. Pass 8 (Strain = 1.5)**

By pass 8, the quantitative data had indicated that precipitation of the  $\beta$ -phase from solution is complete. Some particle coarsening since pass 6 is suggested by the quantitative data, although this is difficult to detect in visual examination of the as-rolled condition of Figure 4.4.a. Continuing spheroidization of particles, however, is apparent. The more homogeneous particle distribution is beginning to inhibit further development of microbands. Compared to pass 6, the annealed condition of Figure 4.4.b reveals increasingly equiaxed and well-defined substructures, especially near larger particles and along prior grain boundaries such as those shown at the bottom of the micrograph. Some features in the upper right corner appear to be very small microbands, but very few of these features remain.

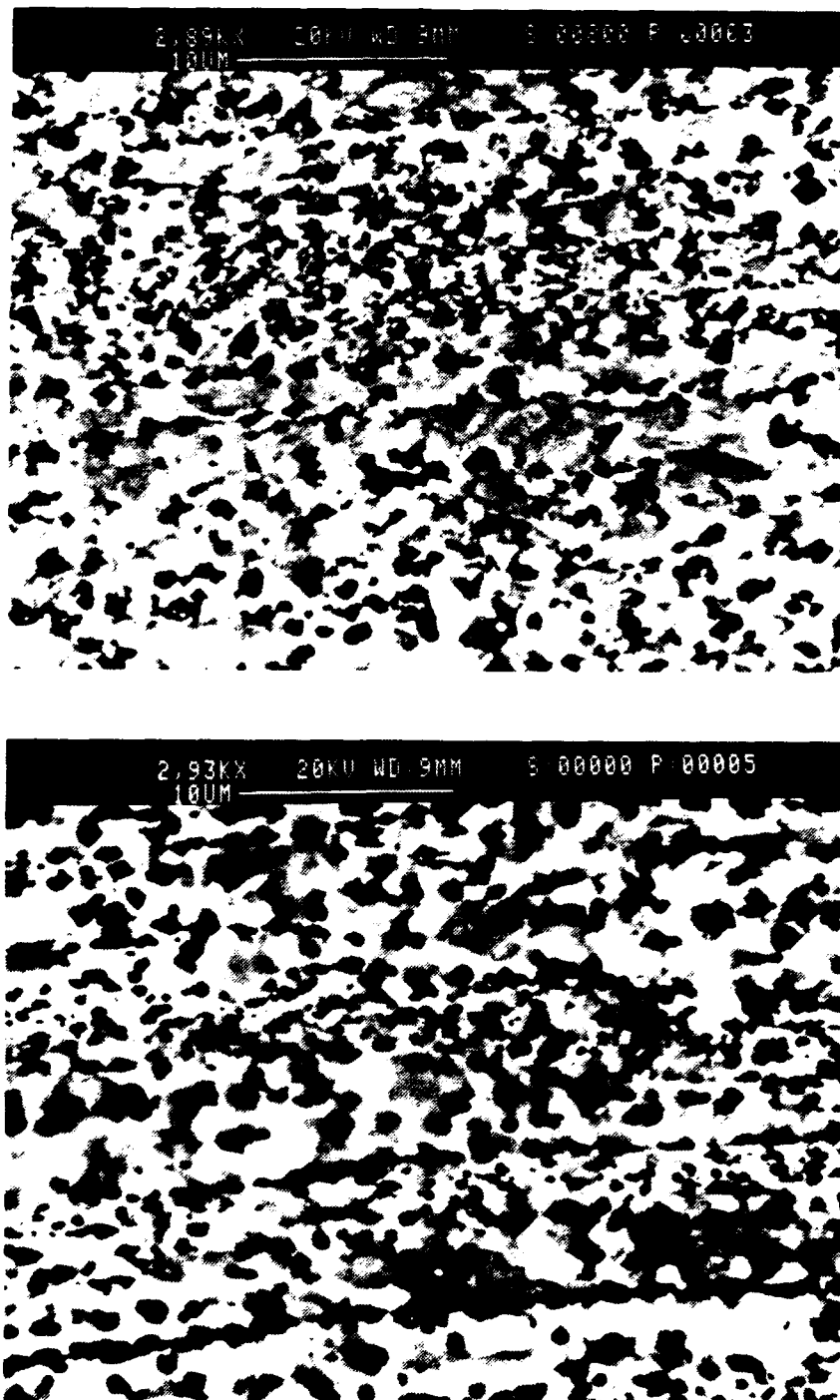


**Figure 4.4.** Backscattered electron micrograph showing Al-10Mg-0.1Zr following pass 8: a) in the as-rolled condition; b) following 30 minutes of annealing at 300 °C

## **5. Pass 10 (Strain = 2.0)**

Mechanical testing by Gorsuch [Ref. 4] showed that this material is capable of superplastic elongations greater than 400% after pass 10. The as-rolled condition in Figure 4.5.a indicates a more homogeneous particle distribution compared to pass 8, although banding of the  $\beta$ -phase particles is still apparent. Linear features - suggesting microbands - are still evident but are not as well-defined as earlier in the processing. In the annealed condition of Figure 4.5.b the microband features are no longer apparent at all. Instead, a uniform and fine equiaxed structure exists. In general, contrast variation is small within the matrix, suggesting that most of these features are recovered structures. Areas adjacent to some particles (at the higher magnification of Figure 4.5.c) show regions of light contrast which may reflect formation of recrystallized grains.

## **6. Pass 12 (Strain = 2.6)**

After the final pass, the material exhibits a refined grain structure, even in the as-rolled condition in Figure 4.6.a. Little, if any, evidence of microbands appears - or at least none that is prominent. The underlying substructure appears to be retained and more equiaxed than that after pass 10.

The annealed condition, Figure 4.6.b, clearly reveals a homogeneous particle distribution with increasing orientation contrast in the fine, equiaxed microstructure. These features range from 1-3  $\mu\text{m}$  in size. Still, there is very little discernible difference between the annealed microstructures following passes 10 and 12. Yet, mechanical testing by Gorsuch [Ref. 4] showed that elongations of 1100% are possible after pass 12, suggesting essentially a fully developed, fine-grained microstructure. To aid in the interpretation of this microstructure, the quantitative data were also obtained.

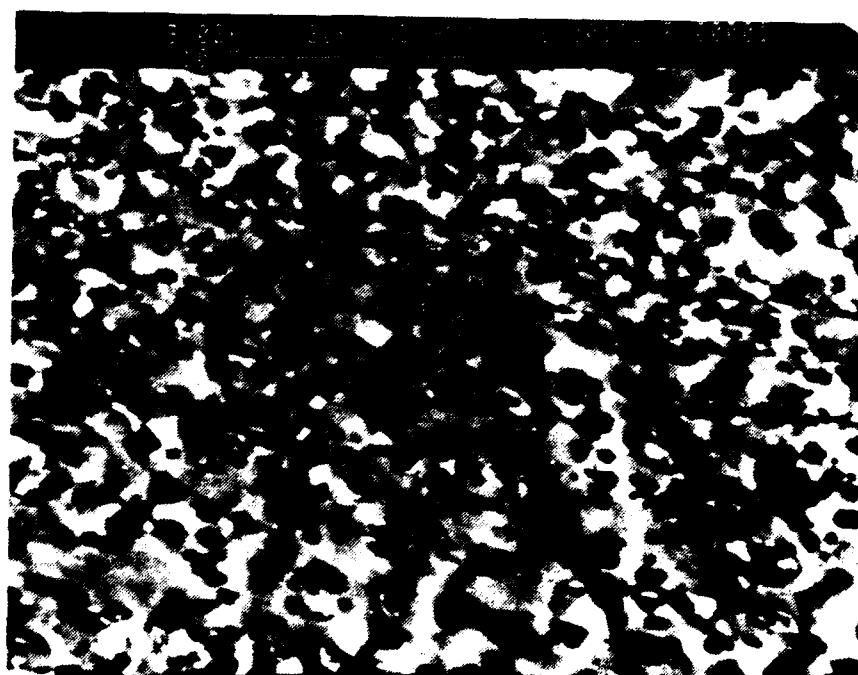


**Figure 4.5.** Backscattered electron micrographs showing Al-10Mg-0.1Zr following pass 10: a) in the as-rolled condition; b) following 30 minutes of annealing at 300 °C.

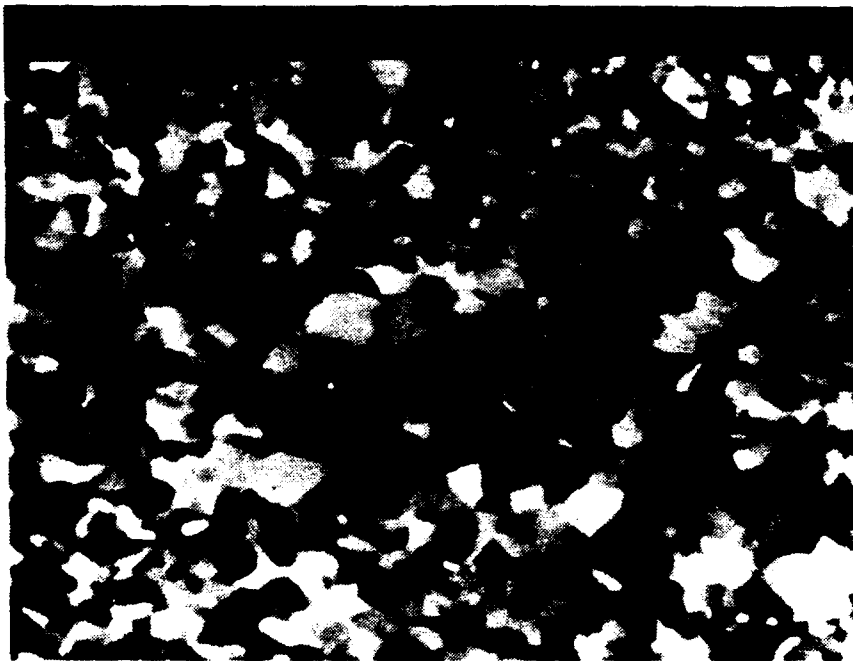


**Figure 4.5.c. Backscattered electron micrograph showing Al-10Mg-0.1Zr following pass 10 in the annealed condition at a higher magnification.**

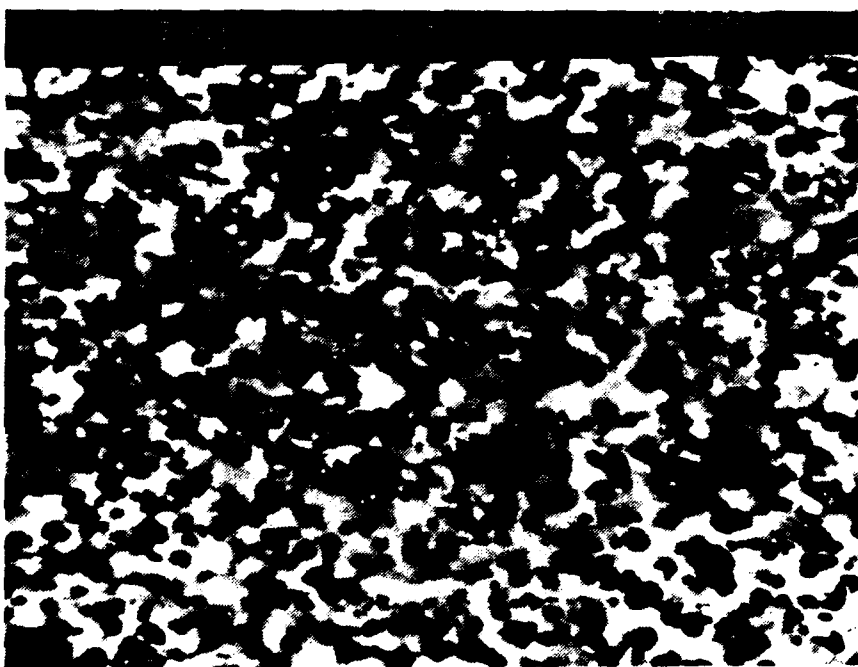
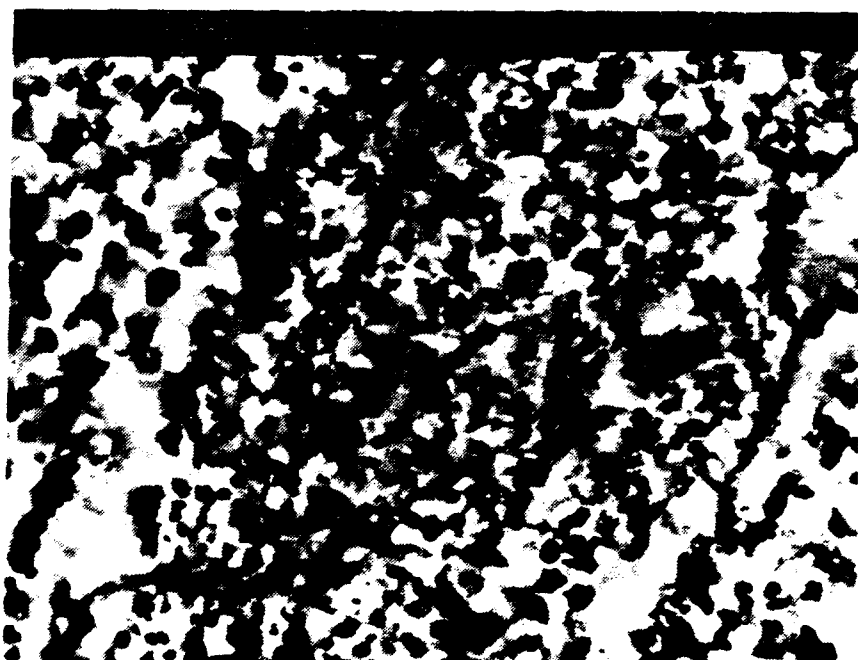


**Figure 4.6.** Backscattered electron micrograph showing Al-10Mg-0.1Zr following pass 12: a) in the as-rolled condition; b) following 30 minutes of annealing at 300 °C.

## B. QUANTITATIVE ANALYSIS

Using the image analysis system previously described, normalized distributions of length, area, perimeter and aspect ratio of the  $\beta$ -phase particles for passes 8, 10 and 12 were generated. Most significantly - and surprisingly - this data revealed that only subtle changes in the  $\beta$ -phase particle size distribution occurred during these latter passes of TMP 6. The tabular data for the histograms is presented in Appendix A.

The length of each particle was determined by measuring the maximum length of a chord rotated incrementally through 180 degrees within the particle. The normalized length distribution shown in Figure 4.7 reveals a very subtle shift in the "hump" of the histogram toward the left. This indicates that the average length is decreasing. This is occurring through the mechanism of spheroidization, a process by which continuous particles are pulled apart with formation of a diffuse neck, eventually separating into more discrete, sphere-like particles. This spheroidization process contributes significantly to the homogenization of the  $\beta$ -phase in the latter passes.

Results of the normalized aspect ratio distribution further support spheroidization of the  $\beta$ -phase particles. The aspect ratio was determined as the maximum chord length divided by the y-axis width of the particle. This accounts for values  $< 1.0$  observed in Figure 4.8. The maximum in these histograms migrates leftward toward a value of 1.0 during processing, indicating very clearly that elongated particles are becoming more sphere-like. This phenomenon is also observable in the microstructure of passes 8, 10 and 12 previously presented.

Figure 4.9 shows the normalized area distribution for passes 8, 10 and 12, respectively. No detectable change in the distribution is evident, indicating that no particle coarsening is occurring after the  $\beta$ -phase has fully precipitated.

The volume fraction of the  $\beta$ -phase was also determined and is plotted versus true strain in Figure 4.10.a. These data apply to the as-rolled condition for each pass and show a steady increase in volume fraction up to pass 8, when precipitation is complete, after which they remain between 9 - 12%. This is the expected range in accordance with the lever rule applied to the Al-Mg phase diagram at  $T = 300\text{ }^{\circ}\text{C}$ , allowing for a range of  $10\text{ }^{\circ}\text{C}$  during processing and for uncertainty in the phase diagram data.

Figure 4.10.b presents the particle length versus true strain for the whole TMP 6 schedule. A gradual increase in mean length occurs up to pass 8, to a value of  $0.66\text{ }\mu\text{m}$ . The length thereafter remains relatively constant, with mean values of  $0.57\text{ }\mu\text{m}$  and  $0.56\text{ }\mu\text{m}$  recorded for pass 10 and 12, respectively. According to Thompson [Ref. 23], as summarized by Vander Voort [Ref. 24], a correction factor must be applied to the mean linear intercept of an areal image analysis to reflect the spatial aspects of the actual grain diameter. Particle mean length must be corrected in the same manner. If particles are assumed to be spherical, then this correction factor is 1.5. Accordingly, the values of mean length become  $0.99\text{ }\mu\text{m}$ ,  $0.86\text{ }\mu\text{m}$  and  $0.84\text{ }\mu\text{m}$  for pass 8, 10 and 12, respectively. It is recognized that the correction factor increases for less spherical particles, but probably does not have significant implications to this research due to the error already inherent to the quantitative data.

The quantitative data clearly indicates that particles are not coarsening after pass 8, even though complete precipitation of the  $\beta$ -phase from solution has apparently occurred by this stage in the TMP.

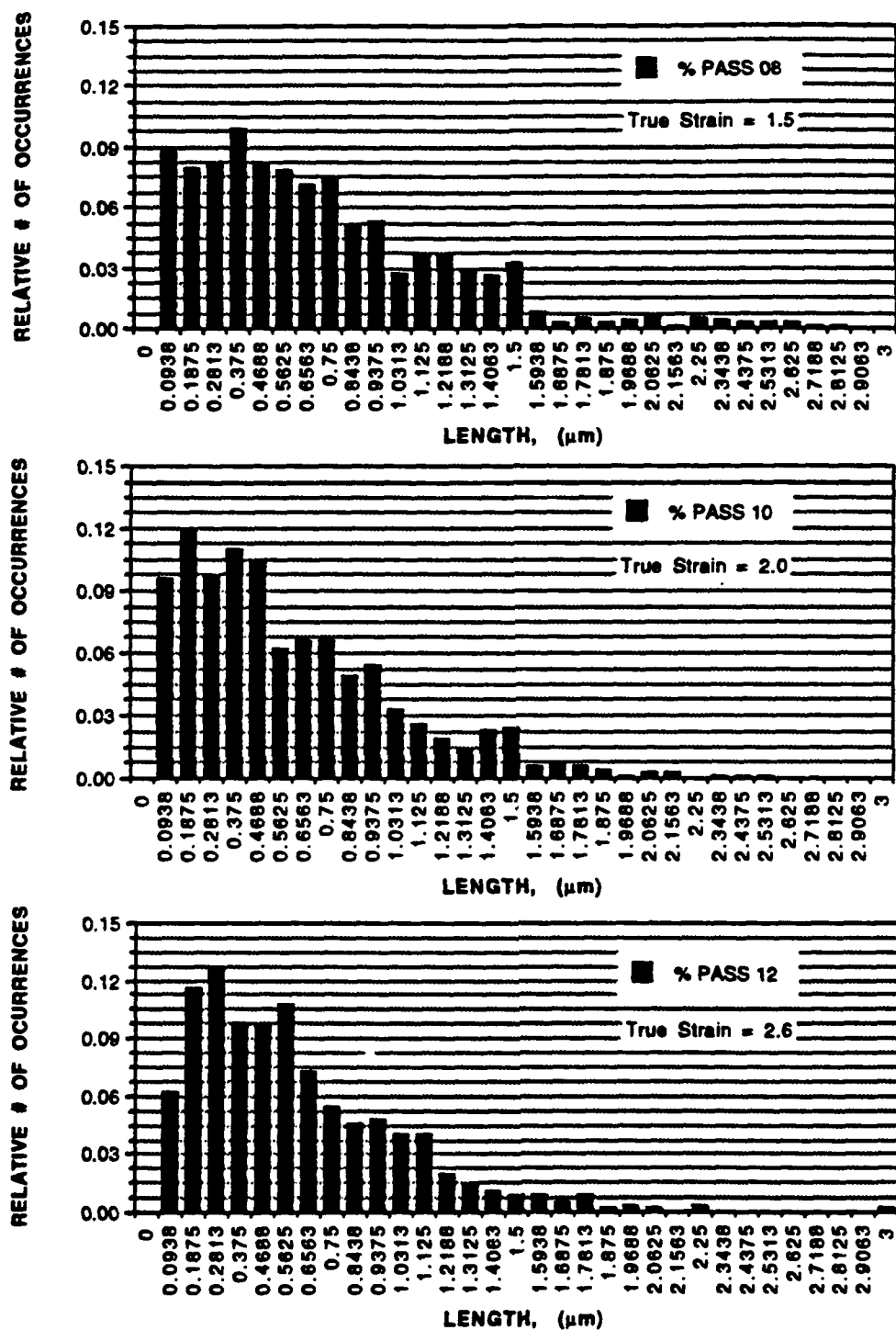


Figure 4.7. Normalized Length Distribution: a) Pass 8; b) Pass 10; c) Pass 12

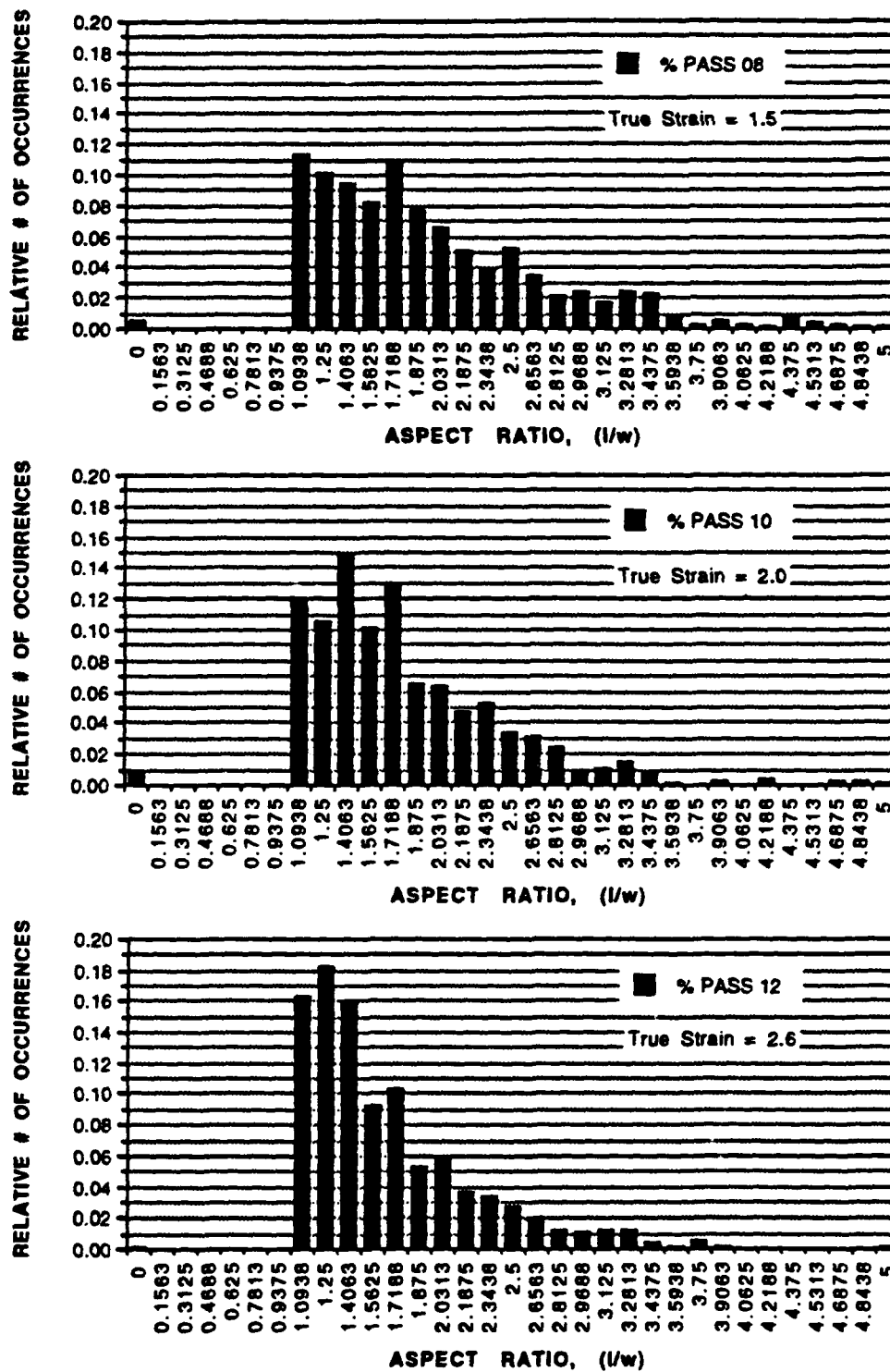


Figure 4.8. Normalized Aspect Ratio: a) Pass 8; b) Pass 10; c) Pass 12

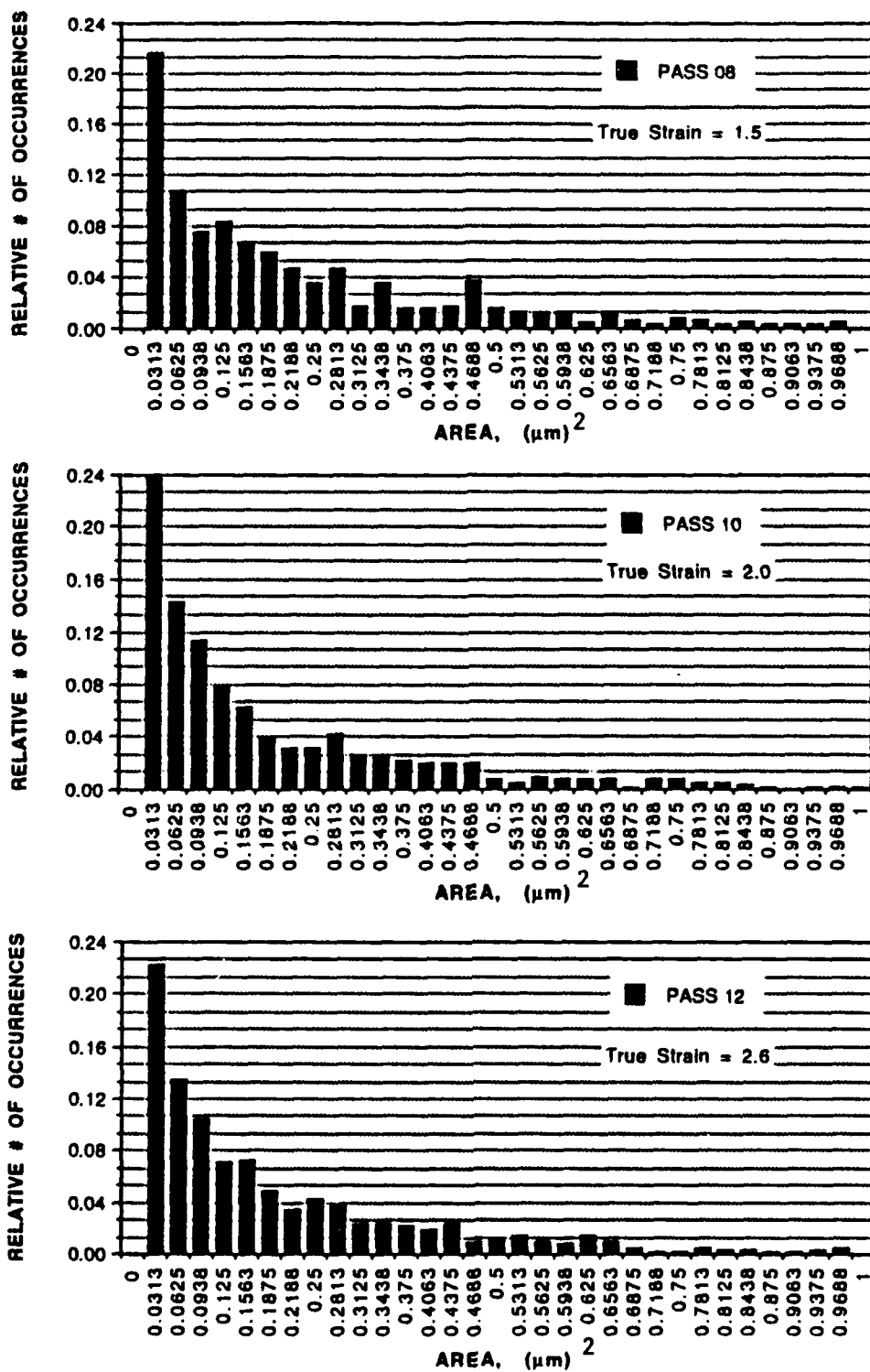
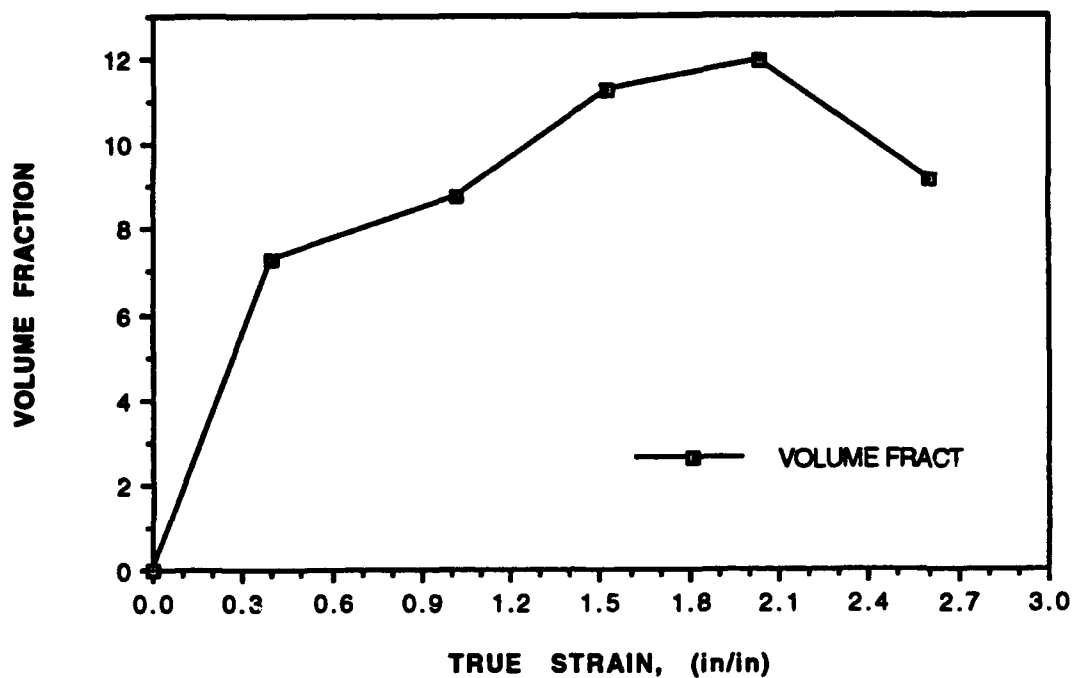
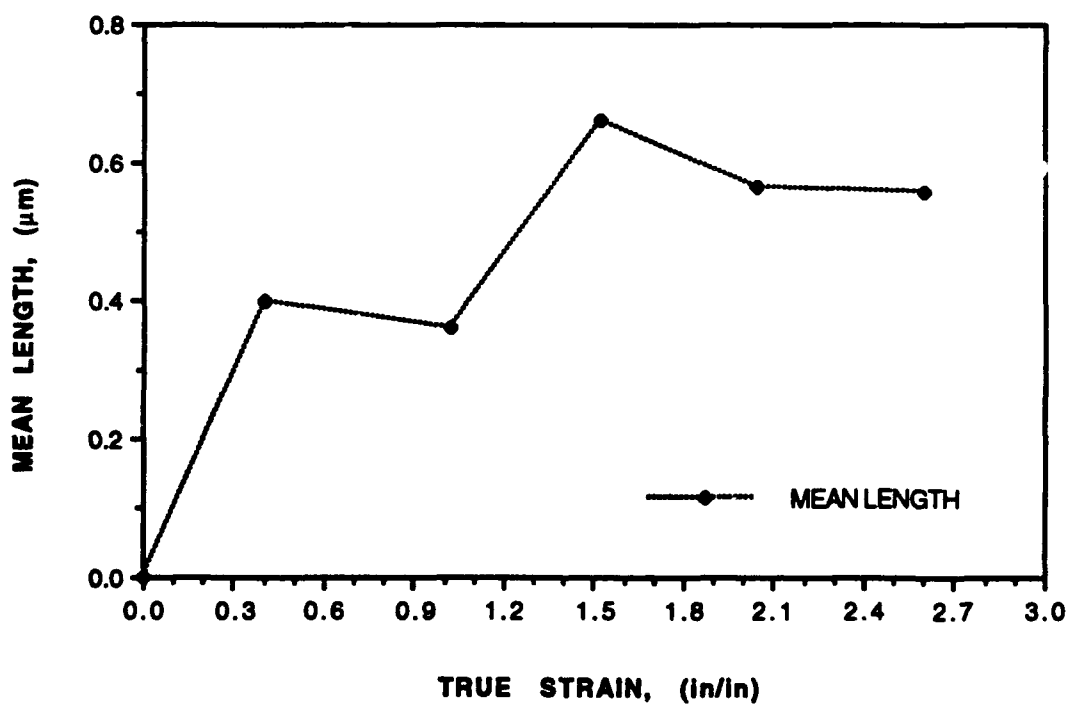


Figure 4.9. Normalized Area Distribution: a) Pass 8; b) Pass 10; c) Pass 12



**Figure 4.10.a. Al-10Mg-0.1Zr  $\beta$ -phase Volume Fraction versus True Strain**



**Figure 4.10.b. Al-10Mg-0.1Zr  $\beta$ -phase Particle Length versus True Strain**

## C. DISCUSSION

Previous mechanical testing by Gorsuch [Ref. 2] on identical material processed under nearly the same conditions has shown elongations of 400% at a strain of 1.9 and 1100% at the final strain of 2.5. The mechanical data suggested that material strained to 1.9 possessed a less fully recrystallized microstructure than that of the material fully processed to a strain of 2.5. Further observations of Gorsuch's fully processed material utilizing backscattered imaging methods on the SEM showed high contrast grains equal in size to the interparticle spacing in fully processed material. This mechanical and microstructural data was interpreted in terms of increased PSN in association with increasing rolling strain. The particle size, a critical factor in PSN, was not evaluated quantitatively in that work. [Ref. 12]

In reviewing the microstructural data presented in this work, the annealed conditions of passes 8, 10 and 12 each reveal fine, equiaxed structures and the differences among them are not very apparent. Furthermore, the quantitative data from the image analysis indicates the same conclusion - particles are not coarsening in the latter passes. There is, however, a gradual change in the as-rolled condition of these passes, described previously as spheroidization during deformation, and supported quantitatively by the decreasing aspect ratio reported earlier. Examining both microstructural and quantitative data indicates particle size and distribution remains essentially fixed at least from a strain of 2.0 to a strain 2.6. Superplastic response seems to develop over this same strain interval and this suggests that it is developing over a range of strain values instead of occurring only after surpassing of a threshold in pass 12. A further indication of this is the hardness data from Lyle [Ref. 22]. Obtained at room temperature for material processed to passes 3, 6, 8, 10 and 12 (both on as-rolled and annealed samples), this hardness data shows the material getting progressively harder, even for the annealed condition over a

sequence of passes. The only exception is for the last pass where hardness dropped for the annealed condition when compared to the annealed condition after pass 10.

In the rolling process used, strain per pass is nearly constant after pass 6; however, the strain rate continuously increases to a maximum on pass 12. The annealing temperature remains constant throughout the process, but as the material gradually thins, two important phenomena occur: 1) the material will reheat more rapidly to 300 °C during annealing, but 2) when removed from the oven, the material will chill (air quench) more rapidly during transfer to the rolling mill. The PSN model developed earlier was considered to apply to a material rolled at room temperature and then subsequently annealed to induce recrystallization. So, direct application of PSN theory to procedures in this work needs to be carefully considered.

The strain per pass, strain rate, volume fraction of  $\beta$ -phase, temperature and particle dispersion for passes 8, 10 and 12 are all very similar. Thus, for any one of these passes, the PSN model - based on strain per pass - could be invoked and one would expect recrystallization to occur successively after each of these passes. This is not the case, at least insofar as superplastic response is concerned. Also, the hardness data reveal increasing hardness and this suggests the accumulation of strain and the absence of recrystallization. In order to apply the PSN model, the accumulated strain must be considered and not simply the strain on the final pass. This is, however, problematic because the PSN model was not developed to treat the problem of recrystallization in a material initially containing a recovered subgrain structure. The Al-Mg alloy in this work apparently does develop such a substructure during the interpass annealing. From pass 6 onward the material appears to form this recovered subgrain structure of size on order of interparticle spacing.

In the PSN model described by Equation (9) in Background, the critical particle diameter depends on the grain boundary interfacial energy,  $\gamma$ , among other

factors. The interfacial energy of a subgrain boundary is less than that of a high angle grain boundary, and so the observation of substructure formation after passes 8, 10 and 12 at least may reflect a "PSN of recovered structures" which appear to be of similar size. However, there simply isn't a good model at present to describe the conditions of nucleation in such a circumstance.

The degree of recrystallization in the last two passes, insofar as particles are concerned, may also reflect the differences in temperature and strain rate in conjunction with the contribution made from the presence of substructure in the material. The increasing strain rate and temperature would act to increase the stored strain energy,  $E$ , available to drive the recrystallization process, even if strain per pass were constant. Then the preexisting subgrains may assist in the formation of high angle grain boundaries simply by reducing the required energy. Instead of needing to provide all the interfacial energy  $\gamma_{\text{high angle}}$  required, only  $(\gamma_{\text{high angle}} - \gamma_{\text{low angle}})$  may be needed to initiate the nucleation event.

The net effect is that, instead of particles coarsening, the critical particle diameter is progressively decreasing and allowing a continuous nucleation to occur over a series of passes. This discussion is not implying a specific mechanism for this, but is simply defining the conditions may lead to heterogeneous nucleation sites within the deformation zones to support the onset of recrystallization.

## **V. CONCLUSIONS AND RECOMMENDATIONS**

### **A. CONCLUSIONS**

The conclusions and observations of this research are as follows:

1. The  $\beta$ -phase of the Al-10Mg-0.1Zr alloy is fully precipitated from solution by pass 8 (strain  $\approx 1.5$ )
2.  $\beta$ -phase particle size distribution remains relatively constant during passes 8-12 of the TMP (strain  $\approx 1.5$ -2.6). Particles do not coarsen after pass 8.
3. Spheroidization of the  $\beta$ -phase particles occurs during processing, approaching an aspect ratio of 1 at the conclusion of pass 12 (strain  $\approx 2.6$ ).
4. Strain accumulates during TMP in the form of recovered substructures associated with the  $\beta$ -phase.
5. The definitive role of the  $\beta$ -phase in recrystallization process is not clear; however, because the grain size appears to become equivalent to the interparticle spacing, it is postulated that the particles act as nucleation sites. As the substructures associated with the  $\beta$ -phase form during processing, they reduce the activation energy for recrystallization and aid its onset.

### **B. RECOMMENDATIONS**

The recommendations for further research are as follows:

1. Conduct further image analysis to include the as-rolled condition of pass 6.
2. Perform a backscattered Kikuchi analysis of the microbands to determine their origin. Analysis should include the misorientation of adjacent bands to assess whether they are twin related.
3. Modify the TMP 6 schedule so that long annealing cycles are employed through pass 7, and shorter annealing cycles are maintained during subsequent passes.

## APPENDIX A

**TABLE 3: NORMALIZED LENGTH TABULAR DATA**

CLASS #	LENGTH ( $\mu\text{m}$ )	# PASS 08	# PASS 10	# PASS 12	NORM. % PASS 08	NORM. % PASS 10	NORM % PASS 12
1	0.0000	0	0	0	0.000	0.000	0.000
2	0.0938	67	67	34	0.087	0.096	0.062
3	0.1875	61	84	64	0.080	0.120	0.117
4	0.2813	63	68	70	0.082	0.097	0.128
5	0.3750	76	77	54	0.099	0.110	0.098
6	0.4688	63	73	53	0.082	0.105	0.097
7	0.5625	60	43	59	0.078	0.062	0.107
8	0.6563	55	46	40	0.072	0.066	0.073
9	0.7500	57	46	30	0.074	0.066	0.055
10	0.8438	39	34	25	0.051	0.049	0.046
11	0.9375	41	38	26	0.054	0.054	0.047
12	1.0313	21	23	22	0.027	0.033	0.040
13	1.1250	28	18	22	0.037	0.026	0.040
14	1.2188	28	13	11	0.037	0.019	0.020
15	1.3125	23	10	8	0.030	0.014	0.015
16	1.4063	20	16	6	0.026	0.023	0.011
17	1.5000	25	17	5	0.033	0.024	0.009
18	1.5938	6	4	5	0.008	0.006	0.009
19	1.6875	2	5	3	0.003	0.007	0.005
20	1.7813	4	4	5	0.005	0.006	0.009
21	1.8750	2	3	1	0.003	0.004	0.002
22	1.9688	3	1	2	0.004	0.001	0.004
23	2.0625	5	2	1	0.007	0.003	0.002
24	2.1563	1	2	0	0.001	0.003	0.000
25	2.2500	4	0	2	0.005	0.000	0.004
26	2.3438	3	1	0	0.004	0.001	0.000
27	2.4375	2	1	0	0.003	0.001	0.000
28	2.5313	2	1	0	0.003	0.001	0.000
29	2.6250	2	0	0	0.003	0.000	0.000
30	2.7188	1	0	0	0.001	0.000	0.000
31	2.8125	1	0	0	0.001	0.000	0.000
32	2.9063	0	0	0	0.000	0.000	0.000
33	3.0000	0	0	1	0.000	0.000	0.002

**Table 4: NORMALIZED ASPECT RATIO TABULAR DATA**

CLASS #	ASPECT RATIO	# PASS 08	# PASS 10	# PASS 12	NORM. % PASS 08	NORM. % PASS 10	NORM. % PASS 12
1	0.0000	4	7	1	0.005	0.010	0.002
2	0.1563	0	0	0	0.000	0.000	0.000
3	0.3125	0	0	0	0.000	0.000	0.000
4	0.4688	0	0	0	0.000	0.000	0.000
5	0.6250	0	0	0	0.000	0.000	0.000
6	0.7813	0	0	0	0.000	0.000	0.000
7	0.9375	0	0	0	0.000	0.000	0.000
8	1.0938	87	84	90	0.114	0.120	0.164
9	1.2500	78	74	100	0.102	0.106	0.182
10	1.4063	72	104	88	0.094	0.149	0.160
11	1.5625	63	71	51	0.082	0.102	0.063
12	1.7188	84	91	57	0.110	0.130	0.104
13	1.8750	59	45	29	0.077	0.064	0.053
14	2.0313	51	44	32	0.067	0.063	0.058
15	2.1875	39	33	20	0.051	0.047	0.036
16	2.3438	30	37	19	0.039	0.053	0.035
17	2.5000	40	24	15	0.052	0.034	0.027
18	2.6563	27	22	11	0.035	0.032	0.020
19	2.8125	17	17	7	0.022	0.024	0.013
20	2.9688	19	7	6	0.025	0.010	0.011
21	3.1250	13	8	7	0.017	0.011	0.013
22	3.2813	19	10	7	0.025	0.014	0.013
23	3.4375	18	6	2	0.023	0.009	0.004
24	3.5938	6	1	1	0.008	0.001	0.002
25	3.7500	2	0	3	0.003	0.000	0.005
26	3.9063	4	2	1	0.005	0.003	0.002
27	4.0625	2	0	0	0.003	0.000	0.000
28	4.2188	1	3	0	0.001	0.004	0.000
29	4.3750	6	0	0	0.008	0.000	0.000
30	4.5313	3	0	0	0.004	0.000	0.000
31	4.6875	2	2	0	0.003	0.003	0.000
32	4.8438	1	2	0	0.001	0.003	0.000
33	5.0000	1	1	1	0.001	0.001	0.002

**Table 5: NORMALIZED AREA TABULAR DATA**

CLASS #	AREA ( $\mu\text{m}$ ) <sup>2</sup>	# PASS 08	# PASS 10	# PASS 12	NORM. % PASS 08	NORM. % PASS 10	NORM. % PASS 12
1	0.0000	0	0	0	0.000	0.000	0.000
2	0.0313	165	167	122	0.215	0.239	0.222
3	0.0625	82	100	74	0.107	0.143	0.135
4	0.0938	57	79	57	0.074	0.113	0.104
5	0.1250	64	55	39	0.084	0.079	0.071
6	0.1563	52	44	40	0.068	0.063	0.073
7	0.1875	45	27	27	0.059	0.039	0.049
8	0.2188	36	22	19	0.047	0.032	0.035
9	0.2500	27	22	23	0.035	0.032	0.042
10	0.2813	35	30	21	0.046	0.043	0.038
11	0.3125	13	17	13	0.017	0.024	0.024
12	0.3438	27	17	13	0.035	0.024	0.024
13	0.3750	12	15	12	0.016	0.021	0.022
14	0.4063	12	14	10	0.016	0.020	0.018
15	0.4375	13	14	13	0.017	0.020	0.024
16	0.4688	28	14	5	0.037	0.020	0.009
17	0.5000	12	5	6	0.016	0.007	0.011
18	0.5313	10	3	8	0.013	0.004	0.015
19	0.5625	8	7	5	0.010	0.010	0.009
20	0.5938	8	5	4	0.010	0.007	0.007
21	0.6250	4	5	8	0.005	0.007	0.015
22	0.6563	8	5	5	0.010	0.007	0.009
23	0.6875	5	1	3	0.007	0.001	0.005
24	0.7188	3	5	1	0.004	0.007	0.002
25	0.7500	6	5	1	0.008	0.007	0.002
26	0.7813	5	3	3	0.007	0.004	0.005
27	0.8125	3	3	2	0.004	0.004	0.004
28	0.8438	4	2	2	0.005	0.003	0.004
29	0.8750	3	1	1	0.004	0.001	0.002
30	0.9063	2	0	1	0.003	0.000	0.002
31	0.9375	3	1	2	0.004	0.001	0.004
32	0.9688	4	1	3	0.005	0.001	0.005
33	1.0000	0	1	0	0.000	0.001	0.000

## LIST OF REFERENCES

1. Sherby, O. D., and Wadsworth, J., "Development and Characterization of Fine-Grain Superplastic Materials," *Deformation, Processing and Structure*, American Society for Metals, 1982.
2. McNelley, T. R. and Garg, A., "Development of Structure and Mechanical Properties in Al-10.2 wt. pct. Mg by Thermomechanical Processing," *Scripta Metallurgica*, v. 18, pp. 917-920.
3. McNelley, T. R., Lee, E. W. and Mills, M. E., "Superplasticity in a Thermomechanically Processed High-Mg, Al-Mg Alloy," *Metallurgical Transactions*, v. 17A, pp. 1035-1041.
4. Gorsuch, T. E., *The Roles of Strain and Reheating Interval in Continuous Recrystallization During the Thermomechanical Processing by Warm Rolling of an Al-Mg Alloy*, Master's Thesis, Naval Postgraduate School, Monterey, California, 1989.
5. *Metals Handbook*, Tenth Edition, v. 2, edited by Davis, J. R., et al., ASM International, 1990.
6. *Metals Handbook*, Desk Edition, American Society for Metals, 1985.
7. Mondolfo, L. F., *Aluminum Alloys Structures and Properties*, Butterworths, London, 1976.
8. Savitskii, S. R., "Effect of Temperature on the Mechanical Properties of Intermetallic Compounds," *Mechanical Properties of Intermetallic Compounds*, ed. J. H. Westbrook, J. Wiley and Sons, pp. 87-120, 1960.
9. Savitsky, E. M., *The Influence of Temperature on the Mechanical Properties of Metals and Alloys*, ed. O. D. Sherby, translated from Russian by D. Sherby, Stanford University Press, pp. 238-252, 1962.
10. McNelley, T. R., and Hales, S. J., "The Roles of Zr and Mn in Processing and Superplasticity of Al-Mg Alloys," *Superplasticity in Aerospace II*, ed. T. R. McNelley and H. C. Heikkinen, The Minerals, Metals and Materials Society, pp. 207-222, 1990.
11. Hales, S. J., McNelley, T. R. and McQueen, H. J., "Recrystallization and Superplasticity at 300 °C in an Aluminum-Magnesium Alloy," *Metallurgical Transactions*, v. 22A, pp. 1037-1047, 1989.
12. Crooks, R., Kalu, P. N. and McNelley, T. R., "Use of Backscattered Electron Imaging to Characterize Microstructures of a Superplastic Al-10Mg-0.1Zr Alloy," *Scripta Metallurgica*, v. 25, pp. 1321-1325, 1991.

13. Humphreys, F. J., "Nucleation of Recrystallization in Metals and Alloys with Large Particles," *1st Riso International Symposium (Denmark)*, p. 35, 1980.
14. Williams, J. C. and Starke, E. A., Jr., "The Role of Thermomechanical Processing in Tailoring the Properties of Aluminum and Titanium Alloys," *Deformation, Processing and Structure*, pp. 279-354, American Society for Metals, 1982.
15. Humphreys, F. J., Miller, W. S. and Djazeb, M. R., "Microstructural Development during Thermomechanical Processing of Particulate Metal-Matrix Composites," *Materials Science and Technology*, v. 6, pp. 1157-1166, 1990.
16. Humphreys, F. J. and Kalu, P. N., "Dislocation-Particle interactions during High Temperature Deformation of Two-Phase Aluminum Alloys," *Acta Metallurgical*, v. 35, no. 12, pp. 2815-2829, 1987.
17. Humphreys, F. J., "Particle Stimulated Nucleation of Recrystallization," *Recrystallization '90*, ed. T. Chandra, The Minerals, Metals and Materials Society, pp. 113-122, 1990.
18. Argon, A. S., Im, J. and Safoglu, R., "Cavity Formation From Inclusions in Ductile Fracture," *Metallurgical Transactions*, v. 6A, p. 825, 1975.
19. Nes, E., "Recrystallization and Grain Growth of Multiphase and Particle Containing Materials," *1st Riso International Symposium (Denmark)*, p. 85, 1980.
20. Coleman, M., *Unpublished Research*, Naval Postgraduate School, Monterey, California, 1992.
21. Beckwith, T. G. and Marangoni, R. D., *Mechanical Measurements, Fourth Edition*, Addison-Wesley Publishing Company, pp. 56-60, 1990.
22. Lyle, P. C., *Correlation of Processing, Microstructure and Superplasticity in an Al-Mg-Zr Alloy*, Master's Thesis, Naval Postgraduate School, Monterey, California, 1992.
23. Thompson, A. W., "Calculation of True Volume Grain Diameter," *Metallography*, v. 5, pp. 366-369, 1972.
24. Vander Voort, G. F., *Metallography Principles and Practice*, p. 465, McGraw-Hill Book Co., 1984.

## INITIAL DISTRIBUTION LIST

- |    |  |   |
|----|--|---|
| 1. | Defense Technical Information Center<br>Cameron Station<br>Alexandria, VA 22304-6145   | 2 |
| 2. | Library, Code 52<br>Naval Postgraduate School<br>Monterey, CA 93943-5002   | 2 |
| 3. | Naval Engineering, Code 34<br>Naval Postgraduate School<br>Monterey, CA 93943-5100   | 1 |
| 4. | Department Chairman, Code ME/Kk<br>Department of Mechanical Engineering<br>Naval Postgraduate School<br>Monterey, CA 93943-5000                    | 1 |
| 5. | Professor T. R. McNelley, Code ME/Mc<br>Department of Mechanical Engineering<br>Naval Postgraduate School<br>Monterey, CA 93943-5000               | 4 |
| 6. | Research Associate Professor R. Crooks, Code ME/Cc<br>Department of Mechanical Engineering<br>Naval Postgraduate School<br>Monterey, CA 93943-5000 | 1 |
| 7. | Dr. Lewis Slotter, Code AIR 931A<br>Headquarters, Naval Air Systems Command<br>Washington D.C. 20361   | 1 |
| 8. | Dr. P. N. Kalu<br>c/o Langley Research Center<br>Mail Stop 188A<br>Hampton, VA 23665-5225  | 1 |

9. CPT Stephen A. Rogers  
1347 Easthill St. S.E.  
North Canton, OH 44720

2